

XMM-NEWTON DATA ANALYSIS OF ISOLATED RADIO-QUIET NEUTRON
STARS 1E 1207.4-5209, RX J0002+6246, RX J0822-4300, CXOU J185238.6+004020

by

ARZU ANKAY

B.S. in Physics, Boğaziçi University, 2001

Submitted to the Institute for Graduate Studies in
Science and Engineering in partial fulfillment of
the requirements for the degree of
Master of Science

Graduate Program in Physics

Boğaziçi University

2007

ACKNOWLEDGEMENTS

I would like to thank my thesis supervisor Prof. Dr. Nihal Ercan for her help and support. I thank Prof. Dr. Metin Arık and Prof. Dr. Gökmen Tektunalı for their fruitful comments. I am also grateful to Dr. Murat Hüdaverdi for assisting on the analysis. Last but not least, I thank my husband Assoc. Prof. Dr. Aşkın Ankaş for his patience and support.

ABSTRACT

XMM-NEWTON DATA ANALYSIS OF ISOLATED RADIO-QUIET NEUTRON STARS 1E 1207.4-5209, RX J0002+6246, RX J0822-4300, CXOU J185238.6+004020

In this thesis, data analysis of X-ray dim radio quiet X-ray pulsar 1E 1207.4-5209 and RX J0002+6246, RX J0822-4300, CXOU J185238.6+004020 which have similar observational characteristics as 1E 1207.4-5209 are represented based on XMM-Newton satellite observations. X-ray spectral analysis of neutron star RX J0002+6246 based on XMM-Newton data is given for the first time. The problems related to the magnetic field and age of X-ray pulsar 1E 1207.4-5209 are discussed and a model is proposed to solve these problems. These four neutron stars have some common physical properties based on their observational data, and hence they may have similar physical evolution. It is shown that all of them have pure black body spectra (in three cases 2 black body components) without power law component. No pulsar wind nebula has been observed around any one of them, which strongly shows that they have low rotational energy loss despite their very small ages. All of these neutron stars are physically connected to shell-type supernova remnants which are younger than $(1-2) \times 10^4$ yr. None of these sources has been detected to emit at any radio frequency. These common spectral properties (and possibly common timing characteristics) of these neutron stars are examined. Their possible physical evolution is discussed and a model is proposed. As a result, it is quite possible that these objects form a new class of neutron stars quite different than the other types.

ÖZET

İZOLE RADYO-SESSİZ 1E 1207.4-5209, RX J0002+6246, RX J0822-4300, CXOU J185238.6+004020 NÖTRON YILDIZLARININ XMM-NEWTON VERİ ANALİZİ

Bu tezde X-ışını sönük radyoda gözükmeyen izole X-ışın pulsarı 1E 1207.4-5209 ve bu cisim ile benzer gözlemsel özellikler gösteren RX J0002+6246, RX J0822-4300, CXOU J185238.6+004020 nötron yıldızlarının XMM-Newton uydusu gözlemlerinin bilgisayarla veri analizi sonuçları sunulmaktadır. RX J0002+6246 nötron yıldızının XMM-Newton verilerine dayanan X-ışın tayfı ilk kez bu tezde verilmektedir. 1E 1207.4-5209 X-ışın pulsarının manyetik alanı ve yaşı ile ilgili problemler tartışılmakta ve bu problemlerin çözümüne yönelik bir model önerilmektedir. Bu dört nötron yıldızının gözlemsel verilerinden ortak fiziksel özelliklere sahip oldukları ve dolayısıyla benzer fiziksel evrime sahip olabilecekleri görülmektedir. Tümüünün de üs yasası icermeyen sadece kara cisim (üç durumda 2 kara cisim bileşeni) iceren tayflara sahip oldukları gösterilmektedir. Bu nötron yıldızlarının hiç birinin etrafında pulsar rüzgar nebulası görülmemektedir ki bu da çok genç olmalarına rağmen dönüş kinetik enerji kayıplarının düşük olduğunu gösterir. Tüm bu nötron yıldızları yaşları $(1-2) \times 10^4$ yıldan daha az olan kabuk-tipli süpernova kalıntılarına bağlıdır. Hiç birinin radyo frekanslarında ışınım yaptığı kaydedilmemiştir. Bu tezde ele alınan nötron yıldızlarının bu ortak tayfsal (ve muhtemelen ortak zamansal) özellikleri incelenmektedir. Olası fiziksel evrimleri tartışılarak bir model önerilmektedir. Sonuç olarak, bu cisimlerin diğer izole nötron yıldızı tiplerinden çok farklı bir sınıf oluşturdukları oldukça muhtemeldir.

TABLE OF CONTENTS

ACKNOWLEDGEMENTS	iii
ABSTRACT	iv
ÖZET	v
LIST OF FIGURES	viii
LIST OF TABLES	xii
LIST OF SYMBOLS/ABBREVIATIONS	xiii
1. INTRODUCTION	1
2. ISOLATED NEUTRON STARS AND PULSARS	2
2.1. On the formation of isolated neutron stars	2
2.2. Magneto-dipole radiation and temporal evolution of pulsars	3
2.3. Cooling of Neutron Stars	5
2.4. Physical Characteristics of New Types of Isolated Neutron Stars and Pulsars	6
2.4.1. X-ray Dim Radio-Quiet Neutron Stars	8
2.5. Observational data on 1207-like neutron stars given in the literature . .	12
2.5.1. 1E 1207.4-5209	12
2.5.2. RX J0002+6246	15
2.5.3. RX J0822-4300	15
2.5.4. CXOU J185238.6+004020	17
3. XMM-NEWTON	18
3.1. Spacecraft	18
3.1.1. Components	18
3.1.2. Structural Design	19
3.1.3. Thermal constraints	20
3.2. Mirrors	21
3.2.1. Introduction	21
3.2.2. Telescope Configuration	22
3.2.3. Optical Design	23
3.2.3.1. Image Quality	25

3.2.3.2.	Effective Area	25
3.2.3.3.	X-Ray Straylight Rejection	25
3.3.	EPIC	26
3.3.1.	Introduction	26
3.3.2.	Chip Geometry	27
3.3.2.1.	MOS CCDs	27
3.3.2.2.	PN CCDs	28
3.3.3.	Operating Modes	28
3.3.4.	Instrument Characteristics	29
3.3.4.1.	Quantum Efficiency	29
3.3.4.2.	Background	30
3.3.5.	Filters and Effective Area	31
3.4.	RGS	32
3.4.1.	Instrument Design	32
3.5.	OM	33
4.	OBSERVATION AND DATA REDUCTION	35
4.1.	Observations	35
4.2.	Data Reduction	37
4.3.	Background Treatment	43
5.	ANALYSIS AND RESULTS	51
5.1.	1E 1207.4-5209	52
5.2.	RX J0002+6246	54
5.3.	RX J0822-4300	57
5.4.	CXOUJ185238.6+004020	60
6.	DISCUSSIONS AND CONCLUSIONS	64
	REFERENCES	69

LIST OF FIGURES

Figure 2.1.	Rotation period (P) versus temporal change of rotation period (\dot{P}).	14
Figure 3.1.	XMM-Newton payload	19
Figure 3.2.	Technical drawing of one of the XMM-Newton telescopes	22
Figure 3.3.	Light path in the XMM-Newton telescope	24
Figure 3.4.	CCD chip layout of EPIC MOS (left) PN (right)	27
Figure 3.5.	Quantum efficiency of the EPIC	29
Figure 3.6.	Example of a light curve badly effected by proton flares	30
Figure 3.7.	Combined effective area of all telescopes	31
Figure 3.8.	Schematic layout of the RGS	33
Figure 4.1.	Light curves and screening levels for flares in 1E 1207.4-5209.	39
Figure 4.2.	Light curves and screening levels for flares in RX J0002+6246.	40
Figure 4.3.	Light curves and screening levels for flares in RX J0822-4300.	41
Figure 4.4.	Light curves and screening levels for flares in CXOUJ185238.6+004020.	42
Figure 4.5.	EPIC PN image of 1E 1207.4-5209 obs. 0155960301.	44
Figure 4.6.	EPIC MOS1 image of 1E 1207.4-5209 obs. 0155960301.	44

Figure 4.7.	EPIC MOS2 image of 1E 1207.4-5209 obs. 0155960301.	45
Figure 4.8.	EPIC PN image of 1E 1207.4-5209 obs. 0155960501.	45
Figure 4.9.	EPIC MOS1 image of 1E 1207.4-5209 obs. 0155960501.	45
Figure 4.10.	EPIC MOS2 image of 1E 1207.4-5209 obs. 0155960501.	46
Figure 4.11.	EPIC PN image of RX J0002+6246.	46
Figure 4.12.	EPIC MOS1 image of RX J0002+6246.	46
Figure 4.13.	EPIC MOS2 image of RX J0002+6246.	47
Figure 4.14.	EPIC PN image of RX J0822-4300 obs. 0113020101.	47
Figure 4.15.	EPIC MOS1 image of RX J0822-4300 obs. 0113020101.	47
Figure 4.16.	EPIC MOS2 image of RX J0822-4300 obs. 0113020101.	48
Figure 4.17.	EPIC PN image of RX J0822-4300 obs. 0113020301.	48
Figure 4.18.	EPIC PN image of CXOUJ185238.6+004020 obs. 0204970201.	48
Figure 4.19.	EPIC MOS1 image of CXOUJ185238.6+004020 obs. 0204970201.	49
Figure 4.20.	EPIC MOS2 image of CXOUJ185238.6+004020 obs. 0204970201.	49
Figure 4.21.	EPIC PN image of CXOUJ185238.6+004020 obs. 0204970301.	50
Figure 4.22.	EPIC MOS1 image of CXOUJ185238.6+004020 obs. 0204970301.	50

Figure 4.23.	EPIC MOS2 image of CXOUJ185238.6+004020 obs. 0204970301.	50
Figure 5.1.	Spectra of 1E 1207.4-5209. (two blackbody and Gaussian absorption lines)(PN-camera).	53
Figure 5.2.	Spectra of 1E 1207.4-5209. (two blackbody and Gaussian absorption lines)(MOS1-camera).	53
Figure 5.3.	Spectra of 1E 1207.4-5209. (two blackbody and Gaussian absorption lines)(MOS2-camera).	54
Figure 5.4.	Spectra of RX J0002+6246. (two component blackbody)(PN-camera).	55
Figure 5.5.	Spectra of RX J0002+6246. (two component blackbody)(PN MOS1 MOS2 cameras).	56
Figure 5.6.	Spectra of RX J0002+6246. (blackbody+powerlaw)(PN-camera). .	56
Figure 5.7.	Spectra of RX J0002+6246. (blackbody+powerlaw) (PN MOS1 MOS2 cameras).	57
Figure 5.8.	Spectra of RX J0822-4300. (two componenet blackbody)(PN-camera).	58
Figure 5.9.	Spectra of RX J0822-4300. (two componenet blackbody)(PN MOS1 MOS2 camera).	59
Figure 5.10.	Spectra of RX J0822-4300. (blackbody+powerlaw)(PN-camera). .	59
Figure 5.11.	RX J0822-4300. (blackbody+powerlaw)(PN MOS1 MOS2 camera).	60
Figure 5.12.	Spectra of CXOUJ185238.6+004020. (blackbody)(PN-camera). . .	61

Figure 5.13. Spectra of CXOUJ185238.6+004020. (blackbody)(PN MOS1 MOS2 cameras).	62
Figure 5.14. Spectra of CXOUJ185238.6+004020. (powerlaw)(PN-camera). . .	62
Figure 5.15. Spectra of CXOUJ185238.6+004020. (powerlaw)(PN MOS1 MOS2 cameras).	63

LIST OF TABLES

Table 2.1.	Data on 1207-like neutron stars given in the literature.	14
Table 4.1.	Log of observations.	36
Table 4.2.	The mean count rate values of each observation and 2.7σ (90%) values.	37
Table 5.1.	Spectral parameters of 1E 1207.4-5209.	52
Table 5.2.	Spectral parameters of RX J0002+6246.	55
Table 5.3.	Spectral parameters of RX J0822-4300.	58
Table 5.4.	Spectral parameters of CXOUJ185238.6+004020.	61

LIST OF SYMBOLS/ABBREVIATIONS

B	Perpendicular component of the surface dipole magnetic field
B_{cyc}	Magnetic field found from cyclotron line
c	Speed of light in free space
D	Linear diameter
d	Distance
\dot{E}	Rate of rotational energy loss
I	Moment of inertia
k	Boltzmann constant
L	Luminosity
L_{bol}	Bolometric luminosity
M_{\odot}	Mass of the Sun
N_H	Neutral hydrogen column density
n	Braking index
P	Rotation period
\dot{P}	Time rate of change in P
R	Radius
T	Temperature
t_{SNR}	Age of supernova remnant
w	Line width
α	Angle between the rotation axis and the magnetic field axis
α_p	Photon index
Ω	Rotational velocity
$\dot{\Omega}$	Time rate of change in Ω
Σ	Surface brightness
$\sigma(E)$	Photo-electric cross-section
τ	Characteristic age
τ_{opt}	Optical depth
χ^2	Chi-squared

ATNF	The Australia Telescope National Facility
AXP	Anomalous X-ray pulsars
CAL	Calibration Access Layer
CCD	Charge Coupled Device
CCF	Current Calibration File
Chandra	Chandra X-Ray Observatory
CTE	Charge Transfer Efficiency
CXB	Cosmic X-ray Background
ESA	European Space Agency
EPIC	European Photon Imaging Camera
FITS	Flexible Image Transport System
FOV	Field Of View
FPA	The Focal Plane Assembly
FPP	Focal Plane Platform
FWHM	Full Width at Half Maximum
GTI	Good Time Intervals
HEW	Half Energy Width
IR	Infrared
MIS	Mirror Interface Structure
MOS	Metal Oxide Semi-conductor
MSP	The Mirror Support Platform
ODF	Observation Data File
OM	Optical Monitor
PSF	Point-Spread Function
PWN	Pulsar Wind Nebula
QE	Quantum Efficiency
RGA	Reflection Grating Arrays
RGS	Reflection Grating Spectrometer
ROSAT	The Roentgen Satellite
SAS	Science Analysis Subsystem

SGR	Soft gamma-ray repeaters
SN	Supernova
SNR	Supernova remnant
SOC	XMM-Newton Science Operations Centre
SSC	Survey Science Centre
SVM	The Service Module
TSS	Telescope Sun Shield
UHB	XMM-Newton Users Handbook
UV	Ultraviolet
XMM-Newton	X-ray Multi-Mirror Mission
XDRQNS	X-ray dim radio quiet neutron stars
XDTNS	X-ray dim thermal neutron stars
ZAMS	Zero age main sequence

1. INTRODUCTION

In this thesis, I give the results of my data analysis of isolated radio-quiet neutron stars 1E 1207.4-5209, RX J0002+6246, RX J0822-4300 and CXOU J185238.6+004020 by presenting the X-ray spectra and data of these sources based on all the relevant XMM-Newton satellite observations.

Among these four neutron stars, 1E1207.4-5209 is the most well observed and examined one. On the other hand, both spectral and timing analysis of the remaining three neutron stars have not been done well as seen from the articles given in the literature. In particular, analysis of the X-ray spectra of radio-quiet neutron star RX J0002+6246 has not been published in any article or book.

In the following chapters, I will also attempt to show the common characteristics of these X-ray sources which may lead to a new type of isolated neutron star and may help in clarifying the physical evolution of such anomalous neutron stars.

2. ISOLATED NEUTRON STARS AND PULSARS

2.1. On the formation of isolated neutron stars

Ordinary stars undergo thermonuclear reactions in their cores beginning from fusion of protons up to formation of Fe-group elements (depending on their mass). As the nucleons in the nuclei of Fe-group elements have the largest binding energy per nucleon among all the elements, thermonuclear reactions do not proceed further during massive stellar evolution. When the hydrostatic equilibrium no longer exists (because of the lack of radiation produced by thermonuclear reactions), the massive star collapses on itself forming a compact object. If mass of the compact object does not exceed $3.2 M_{\odot}$ (Fang and Ruffini 1983) the degeneracy pressure of the neutrons formed by inverse beta-decay (neutronization) can balance the gravitational pressure and a neutron star is born. Mass measurements of neutron stars in binary systems (see e.g. Charles and Coe 2003) show that their mass-number distribution has a peak around $1.4 M_{\odot}$, that is close to the Chandrasekhar limit. Radius of a neutron star is usually adapted as 10 km, though it may change in an interval 9-16 km depending on the mass and the equation of state of the neutron star (Shapiro and Teukolsky 1983). The average density of a neutron star must be comparable to nuclear density (on the order of 10^{14} gr/cm³) because of neutronization.

In other words, basically neutron stars are formed as the end product of massive stellar evolution during core collapse supernovae (SNe). Isolated stars (or the ones in wide binaries) with zero age main sequence (ZAMS) mass greater than about $8 M_{\odot}$ end their evolution by core collapse SNe forming neutron stars (Lipunov 1992; Lyne and Graham-Smith 2006) and possibly black holes (the ZAMS mass must be greater than about 25 Solar mass for black hole formation). If the star is in a close binary system, the boundary limits on mass of the progenitor may be larger.

Dominant number of stars are in binary systems as known observationally. Despite this fact, most of the neutron stars are isolated, which shows that there occurs

disruption of the binary system (asymmetric explosion) during most of the core collapse SN explosions. High space velocity of neutron stars (about 250-300 km/s on average, Allakhverdiev et al. 1985; Hansen and Phinney 1996) also supports the asymmetric explosion scenario. On the other hand, the degree of asymmetry is not supposed to be large as the kinetic energy of a newborn neutron star with conventional mass ($1.4 M_{\odot}$) and the energy needed to disrupt the binary system (for average values of companion mass and binary separation) to be on the order of 10^{48} erg is sufficient to form an isolated neutron star with space velocity about 250-300 km/s. This amount of energy is 2-3 orders of magnitude smaller than core collapse SN explosion energy which is typically on the order of 10^{50-51} erg (excluding the kinetic energy of neutrinos formed during the collapse which is about 10^{53} erg).

Today, isolated neutron stars are divided into several subgroups according to their observational (physical) characteristics. Although, there is no common consensus on the number and the names of these subgroups, we can classify them according to their radiation as: radio and/or X-ray pulsars, X-ray dim radio quiet neutron stars (XDRQNSs), X-ray dim thermal neutron stars (XDTNSs), anomalous X-ray pulsars (AXPs) and soft gamma-ray repeaters (SGRs). Among these different types of isolated neutron stars, the most well examined and relatively well understood one is the class of radio pulsars, though there still exist some problems on understanding the physics of them (e.g. varying pulse profiles, nulling, glitches, magnetic field evolution etc.). A radio pulsar is simply a neutron star which is a rotating magnetic dipole. When a massive progenitor star collapses on itself after finishing thermonuclear fusion reactions up to Fe-group elements, its surface dipole magnetic field increases as its radius decreases. Assuming that the magnetic moment of the progenitor star is conserved during the collapse, one can easily estimate the order of magnitude of the surface dipole magnetic field of a newborn neutron star which is on the order of 10^{12} G on average.

2.2. Magneto-dipole radiation and temporal evolution of pulsars

There are two basic observable quantities of isolated pulsars: the rotation period P and the time rate of change of the rotation period \dot{P} . Time rate of change of the

rotational kinetic energy of a rigid body is

$$\dot{E} = I\Omega\dot{\Omega} = \frac{4\pi^2 I \dot{P}}{P^3} \quad (2.1)$$

where I is the moment of inertia and $\Omega=2\pi/P$ is the rotational velocity. The component of the dipole magnetic field of pulsar which is perpendicular to the rotation axis also depends on P and \dot{P} :

$$B = \left(\frac{3c^3 I P \dot{P}}{8\pi^2 R^6}\right)^{1/2} \quad (2.2)$$

where c is the speed of light in free space and R is the radius of pulsar (Shapiro and Teukolsky 2004).

If we assume that the time rate of change of the rotational velocity of pulsar can be expressed as a simple power law (Lyne and Graham-Smith 2006):

$$\dot{\Omega} = -k\Omega^n \quad (2.3)$$

where k is a proportionality constant and the power n is called the 'braking index', then the real age of pulsar can be represented in terms of P and \dot{P} as:

$$t = \frac{P}{(n-1)\dot{P}} \left[1 - \left(\frac{P_0}{P}\right)^{n-1}\right] \quad (2.4)$$

where P_0 is the initial rotation period of pulsar. If P_0 is much less than P:

$$t \cong \frac{P}{(n-1)\dot{P}} \quad (2.5)$$

Magneto-dipole radiative power of pulsars is

$$L = \frac{B_p^2 R^6 \Omega^4}{6c^3} \text{Sin}^2 \alpha \quad (2.6)$$

where B_p is the strength of the dipole magnetic field at the magnetic pole and α is the angle between the rotation axis and the magnetic axis (Shapiro and Teukolsky 2004; Lipunov 1992). If \dot{E} (eqn. 1.1) is equal to L (eqn. 1.6) (i.e. if the net torque on pulsar is equal to the magneto-dipole radiation torque), then the braking index turns out to be $n=3$ (assuming also that eqn.(3) can be applied to express the rotational evolution of pulsar). In such a case, the characteristic age (τ) of pulsar is defined using the $n=3$ condition in eqn.(5):

$$\tau \cong \frac{P}{2\dot{P}} \quad (2.7)$$

So, when $n=3$ and $P_0 \ll P$, τ is approximately equal to the real age of pulsar. When n is greater (less) than 3, τ is greater (less) than the real age. So, if there are extra torques on pulsar which spin it down in addition to the effect of the magneto-dipole radiation torque, the pulsar will evolve with larger \dot{P} values compared to the case of pure magneto-dipole radiation torque. On the other hand, if there is B-decay, the \dot{P} values the pulsar has throughout the evolution will be smaller. Note that the braking index n should be adapted as the average braking index (\bar{n}) of pulsar when considering long time intervals in pulsar's lifetime, because the value of 'instantaneous' (i.e. considering very short time intervals compared to the lifetime of pulsar) braking index may change in time in a complicated way in general.

2.3. Cooling of Neutron Stars

When a neutron star is formed by core-collapse SN of a massive star, its interior temperature must be about 10^{11} K (for thermonuclear reactions to proceed up to formation of Fe-group elements, the core temperature of a massive star should be at least $\sim 10^9$ K). This temperature drops down to 10^{9-10} K very rapidly and then the young neutron star cools down via neutrino cooling in the first 10^{5-6} yr (depending on the equation of state and the mass of neutron star) predominantly, after which photon cooling becomes dominant when the temperature in the interior part of the neutron star is as low as 10^8 K (i.e. when the surface temperature is 10^5-10^6 K, Tsuruta 1974,1979; Malone 1974; Shapiro and Teukolsky 2004). So, for all neutron

stars physically connected to SNRs (lifetime of SNRs is about 10^{4-5} yr depending mainly on the SN explosion energy and the ambient medium in which the SNR's shock wave expands), neutrino cooling should be dominant and their surface temperature must be greater than a few times 10^5 K. If there is a hot spot on the surface of neutron star (possibly on the magnetic poles) it is observed as an X-ray pulsar emitting thermal (black body) radiation.

Besides thermal emission, there will be synchrotron (power-law) emission of pulsar as discussed above briefly. Both thermal and non-thermal components of a neutron star's radiation may or may not be observable depending on its surface temperature, distance from the Sun, position in the Galaxy, observed flux, angle between the rotation and the magnetic axes, beam width of the pulsed emission, surface magnetic field and rotation period.

Most of the detected isolated pulsars are not observed to emit thermally as their surface temperatures are too low and/or their distances from the Sun are in general large. On the other hand, most of the detected young pulsars are observed to have both power-law and black body emission. The neutron stars under consideration in this thesis are all young and physically connected to supernova remnants (SNRs) but they do not have power-law components in their spectra (none of them has been detected at radio frequencies) as the best fits to their X-ray spectra are consisted of one or two black body components only. Possible reasons and consequences of this observational fact will be discussed below.

2.4. Physical Characteristics of New Types of Isolated Neutron Stars and Pulsars

XDRQNSs, XDTNSs, AXPs and SGRs are relatively new classes of isolated neutron stars. None of them have been yet detected in radio frequencies. Some of the XDRQNSs and XDTNSs and all the AXPs and SGRs detected up to date show themselves as X-ray pulsars. AXPs and SGRs should be considered as a single class as they seem to have similar spectral and temporal properties. Gamma-ray bursts have been

observed from SGRs and recently AXPs have been observed to experience X-ray bursts (Kaspi et al. 2003) which further supports the idea that they belong to different phases of the same type of neutron star as predicted by Guseinov et al. (2003a). AXPs/SGRs have long P and high \dot{P} and unlike radio pulsars these objects are not rotation powered pulsars as their \dot{E} values are less than their persistent X-ray luminosity. In order to explain the position of AXPs/SGRs on a $P-\dot{P}$ diagram as well as the source of their persistent X-ray emission and bursts, several 'magnetar' models depending on very high magnetic field have been suggested since 1992 (Duncan and Thompson 1992; see also Thompson and Duncan 1995,1996). On the other hand, it is not possible to explain all the observational characteristics of these sources based on a possible very high magnetic field only (Guseinov et al. 2003a). The idea of possible existence of low mass neutron stars have been proposed by Guseinov et al. (2005a,2005b) to explain their positions on the $P-\dot{P}$ diagram, their very hot surfaces as compared to their ages as found from their physical connections to SNRs, and the gamma-ray and X-ray bursts based on magnetic reconnection. The main difference between this model and the magnetar models is that in such a low mass neutron star model the magnetic field is not supposed to be as high as in the magnetar models ($\leq 10^{14}$ G). This approach leads to a smooth distribution in the surface magnetic fields of isolated neutron stars as a whole.

XDTNSs, as the name suggests, are observed to emit pure thermal radiation without any power law component (Haberl 2005). They have long rotation period (several seconds) and moderate \dot{P} values (see Figure 2.1). Since these objects have low X-ray luminosity the observed ones are located not so far away from the Sun ($d < 500$ pc). Yet, their number in such a relatively small volume around the Sun leads to a high birth rate for this type of isolated neutron star (Guseinov et al. 2005c). Some of XDTNSs may be descendants of AXPs/SGRs and/or they may evolve from normal radio pulsars.

XDRQNSs is not a well defined subclass; some of these sources are called in some references as "central compact objects" as they are physically connected to SNRs (but note that there are some other isolated neutron stars as central compact objects of

some SNRs, which are certainly not XDRQNSs). The locations of XDRQNSs on the $P-\dot{P}$ diagram may be in the region where bulk of the radio pulsars are present, but this is not so clear as the number of such sources with measured P and \dot{P} values is very limited.

The best known example of XDRQNSs is 1E 1207.4-5209 which is one of the most heavily examined neutron star among all the types up to date . Although, it is located in the bulk pulsar population on the P - \dot{P} diagram, its observational characteristics are quite different compared to normal radio and/or X-ray pulsars. We will use this source as a model in this thesis to distinguish the sources which belong to the class of XDRQNSs. Spectral analysis of this source as well as RX J0822-4300, CXOU J185238.6+004020 and RX J0002+6246, which have observational characteristics similar to 1E 1207.4-5209, based on the XMM-Newton data will be presented in chapters 4 and 5.

2.4.1. X-ray Dim Radio-Quiet Neutron Stars

None of the XDRQNSs, XDITNSs or AXPs/SGRs has been detected at radio frequencies with the exception AXP XTE J1810-197 from the direction of which radio emission at 1.4 GHz has been detected (Halpern et al. 2005), but this radio emission might also be produced by a possible pulsar wind nebula (PWN) around this AXP.

There are only a few observationally known XDRQNSs. All of them are physically connected to Galactic SNRs which are located up to about 3.5 kpc from the Sun and which have ages about $(3-20) \times 10^3$ yr with the exception of about 320 yr old SNR Cassiopeia A which is one of the most heavily examined SNR especially because of its very high radio surface brightness and the SN explosion energy (Guseinov et al. 2004a,2005c).

Although, none of the XDRQNSs has been detected at radio frequencies, this does not necessarily mean that they have no radio emission. There are basically two selection effects (other than the background radiation which is effective only on the

sources located in the Galactic central directions, see Ankay et al. 2004) which can prevent detection of the radio emission: the beaming fraction and the luminosity function. Based on radio pulsar observations, there exists a strong evidence that beaming fraction decreases in time possibly because of the angle between the rotation axis and the magnetic axis (α) decreasing during the evolution (Tauris and Manchester 1998). Indeed, the existence of B-decay (where B is the component of the dipole magnetic field perpendicular to the rotation axis) for a large sample of pulsars was shown by Guseinov et al. (2004b) by comparing the characteristic ages of pulsars with their kinematic ages (i.e. their distances from the Galactic plane). Guseinov et al. (2004b) assumed an exponential decay with a characteristic decay time $\tau_d=3\times 10^6$ yr. The cause of B-decay in the case of pulsars can be a temporal decrease in α , but the possibility of a decay in the dipole magnetic field itself can not be totally excluded (see e.g Geppert & Rheinhardt 2002 on the possibility of magnetic field decay in neutron stars).

The other selection effect is related to radio luminosity versus number distribution of pulsars (luminosity function). Based on the observational data, most of the pulsars must have low radio luminosity at birth and the radio luminosity, which is only a small fraction of the magneto-dipole radiation produced by the pulsar, does not change significantly in time (Guseinov et al. 2003b).

As mentioned above, all the known XDRQNSs are connected to Galactic SNRs with ages $\leq 2\times 10^4$ yr. Most of the Galactic SNRs are shell-type (Green 2006) and many of these SNRs lack detected point sources or PWNe in them. Direct detection of neutron stars in many of the SNRs may not be possible because of the selection effects and the large distances. On the other hand, PWN is not seen around pulsars which have rate of rotational energy loss $\dot{E}<10^{35}$ erg/s (Guseinov et al. 2004c). The only known XDRQNS with measured P and \dot{P} values is 1E 1207.4-5209 and it has $\dot{E}=2\times 10^{34}$ erg/s. This explains why there is no PWN around 1E 1207.4-5209.

Most of the observed neutron stars show themselves as radio pulsars. In ATNF pulsar catalogue, there are more than 1700 neutron stars and about 80% of them are radio pulsars. On the other hand, most of the observed isolated pulsars rotate rapidly

with $P > 1$ s. Obviously, such rapidly rotating objects should be neutron stars as white dwarfs and ordinary stars can not have such rapid rotation without disrupting. Magnetars (AXPs/SGRs) and XDTNSs which have $P > 1$ s are exceptions in this sense, but these objects are surely neutron stars (not white dwarfs) as their surface temperature, luminosity and surface magnetic field are too high for any white dwarf.

On the other hand, some isolated neutron stars do not show themselves as pulsar in any low or high frequency band. Such objects are identified as neutron stars by their L_x/L_{opt} ratio to be high as compared to normal stars and/or from their positional coincidence with geometric centers of SNRs (in some cases "bow shock" or PWN in the central part of an SNR further supports a physical connection between the NS and the SNR which are in the same direction).

XDRQNSs (otherwise known as "compact central objects" in some articles) examined in this thesis are 1E 1207.4-5209 ($P=424$ ms, $\dot{P} \cong 1.4 \cdot 10^{-14}$, $d=2$ kpc, SNR G296.5+10.0), RX J0822-4300 ($P=220$ ms (?), $d=2$ kpc, SNR Puppis A), CXOU J185238.6+004020 ($P=105$ ms, $d \cong 7$ kpc, SNR Kes79) and RX J0002+6246 ($P=242$ ms (?), $d \cong 3.5$ kpc, SNR 117.7+0.6). Only 1E 1207.4-5209 and CXOU J185238.6+004020 have been observed as X-ray pulsars. For RX J0822-4300 and RX J0002+6246 the measured P values have not been confirmed yet.

These four neutron stars have some common physical properties based on their observational data, and hence they may have similar physical evolutions. All of them have pure black body spectra (in three cases 2 black body fits) without power law component. No PWN has been observed around any one of them, which is an evidence that they have low \dot{E} even though they are very young (\dot{E} has been measured only for 1E 1207.4-5209 yet). All of them are physically connected to S-type SNRs which are younger than $(1-2) \times 10^4$ yr (which are also the ages of these neutron stars). None of these sources has been detected to emit at any radio frequency.

There are also some other physical properties which may be common for this type of neutron stars (we will name them simply as "1207-like" objects), but up to

date only 1E 1207.4-5209 has been detected to have them: characteristic age (τ) of 1E 1207.4 is much larger than age of its SNR which suggests that there is a rapid B-decay for this source. Absorption lines have been clearly observed in its X-ray spectrum which is very uncommon among isolated neutron stars as their atmosphere must be geometrically very thin (in fact 1E 1207.4-5209 is the only such neutron star among the isolated ones, for neutron stars in binaries such absorption lines are common because of the plasma around them as a result of mass accretion from the companion star in a close binary system). The ratio L_X/\dot{E} is large (~ 0.1) compared to normal radio/X-ray pulsars. There are anomalous oscillations in \dot{P} of 1E 1207.4-5209 which are certainly not glitches.

It must also be noted that two other neutron stars may be 1207-like objects: RX J0852.0-4622 (SNR G266.2-1.2) and CXO J2323+5848 (SNR Cas A). In order to test whether these neutron stars have properties similar to 1E 1207.4-5209 further observations are needed.

Two other sources which are given as compact central objects in some articles are not 1207-like: RX J0007.0+7302 has PWN around it and it has synchrotron emission (Halpern et al. 2004; Slane et al. 2004). Although, this neutron star has not been observed as a pulsar, its observational data are similar to the data of young isolated neutron stars. Also, 1E 161348-5055 has been claimed as a central compact object of SNR RCW 103 in the literature (see e.g. Reynoso et al. 2004). Long term variability (several hours) and eclipsing of its X-ray emission strongly suggests that this is a low-mass X-ray binary and the connection of this neutron star to the SNR is not real (chance projection).

Below, the observational data on 1E 1207.4-5209 and 1207-like neutron stars will be represented, the physical characteristics mentioned above will be discussed and an evolutionary model for these anomalous neutron stars will be suggested.

2.5. Observational data on 1207-like neutron stars given in the literature

The observational data given in the literature on the XDRQNSs under consideration are displayed together with brief discussions in this chapter. A detailed representation and the results of the data analysis of these sources done in this thesis will be given in Chapter 4 and Chapter 5.

2.5.1. 1E 1207.4-5209

Dim radio-quiet neutron star (DRQNS) 1E 1207.4-5209 has been examined by both XMM-Newton and Chandra X-ray satellites. The Chandra observation of this X-ray pulsar in 2000 revealed the X-ray pulsar (and hence neutron star) nature of this source ($P=424$ ms). In this observation, two wide absorption lines centered at 0.7 and 1.4 keV have also been detected. In addition to these lines two other absorption lines centered at 2.1 and 2.8 keV have been seen in the spectrum of 1E 1207.4-5209 in the 300 ks XMM-Newton observation. This looks like a harmonic series with a principal frequency at 0.7 keV and its harmonics at 1.4, 2.1 and 2.8 keV. On the other hand, there is an intrinsic atomic transition for both Chandra and XMM-Newton detectors around 2.1 keV that this line may simply be detectors' noise. Another problem is related to the line at 2.8 keV detected by XMM-Newton; this absorption line is not so clear compared to the other lines, though it may still be statistically significant.

If these absorption lines do actually form a harmonic series, then the principal line can be formed by resonant proton cyclotron scattering leading to a surface magnetic field about 1.4×10^{14} Gauss, which is two orders of magnitude larger than the perpendicular component of the surface dipole magnetic field (B) found from the rotation period (P) and the time rate of change in the rotation period (\dot{P}) of 1E 1207.4-5209.

There is also another significant problem based on the observational data of this X-ray pulsar and its SNR. Age of the SNR G296.5+10.0 which is physically connected to 1E 1207.4-5209 is two orders of magnitude smaller than the characteristic age ($\tau=P/2\dot{P}$) of the neutron star. Discrepancies in the magnetic field and age values may be explained

based on a simple exponential B-decay model as shown by Ankay et al. (2007). Such a model may also help us to understand the lack of detected radio emission from this source (and possibly from some other radio-quiet sources) and also to explain the lack of point sources and PWNe in most of the SNRs observed up to date (in Green's catalogue of Galactic SNRs, only 9 and 30 SNRs are F and C type, respectively, among all the 265 known SNRs).

In Figure 2.1, P- \dot{P} diagram for different types of isolated pulsars is displayed. In this figure, small dots represent radio pulsars. Symbols 'cross' and 'star' denote AXPs-SGRs and XDTNSs, respectively (upper limits on \dot{P} for 3 XDTNSs are shown by arbitrary arrows). The actual position of 1E 1207.4-5209 is shown by a 'dark square' and its position for n=3 case (see text) is displayed by a 'plus' sign. Constant lines of B, \dot{E} and τ are denoted by B11-B15, E29-E41 and T3-T9, respectively. Some points on the evolutionary tracks found from the exponential B-decay model (see text) are displayed as 'light squares': a,b,c ($B_0=2\times 10^{13}$ G, $\tau_d=2.5$ kyr); d,e,f ($B_0=2\times 10^{13}$ G, $\tau_d=5$ kyr); g,h,i ($B_0=4\times 10^{13}$ G, $\tau_d=2.5$ kyr); j,k,l ($B_0=4\times 10^{13}$ G, $\tau_d=5$ kyr). (This figure is from Ankay et al. 2007)

The characteristic decay time (τ_d) for radio pulsars based on exponential decay was found to be on the order of 10^6 years (Guseinov et al. 2004b), whereas τ_d of 1E 1207.4-5209 seems to be only several thousand years (see Figure 2.1). Such a rapid decay leads to a short lifetime for 1E 1207.4-5209 and similar neutron stars. In Table 2.1, candidates for 1207-like neutron stars are represented together with their available observational data. All the neutron stars in this table are physically connected to SNRs and their ages (i.e. the ages of their SNRs) are not larger than $(1-2)\times 10^4$ years. None of these sources have PWNe around them and this observational fact can also be explained by a rapid B-decay (i.e. a rapid decrease in \dot{E} which is the main physical parameter for formation of PWN, see Guseinov et al. 2004c). The only such neutron star with measured P and \dot{P} values is 1E 1207.4-5209 so that timing measurements of other sources are essential to test the applicability of the B-decay model further.

2.5.2. RX J0002+6246

$P=242$ ms was measured from ROSAT observations (Hailey and Craig 1995) which has yet to be confirmed by precise timing observations.

RX J0002+6246 is connected to G117.7+0.6 which is given as a probable SNR in Green (2006). G117.7+0.6 was observed as a partial shell which may be the remnant of a previous SN that swept up the region of SNR CTB 1. G117.7+0.6 may have a distance of about 3-4 kpc as it is located in the direction of the Perseus arm, probably in a very dense medium. Its $N_H=8\times 10^{21}$ similar to CTB1 which has $N_H=7\times 10^{21}$ (Hailey and Craig 1995) that these 2 SNRs may be in the same region.

There is no PWN around this young neutron star and if $P = 242$ s then $\tau \gg t_{SNR}$ ($t_{SNR} = 10\text{-}20$ kyr).

2.5.3. RX J0822-4300

The distance to this source (i.e. the distance to its SNR) was measured to be: $d=2$ kpc (Petre et al. 1996; Guseinov et al. 2004a) and $d=2.2$ kpc (Reynoso et al. 1995; Green 2006; Hui and Becker 2006a,2006b). In this work, $d=2$ kpc is adapted. The proper motion measurements of this neutron star led to a very high transverse velocity, $V(\text{transverse}) = 1122\pm 360$ km/s (for $d=2.2$ kpc, Hui and Becker 2006b). This should be checked by further observations.

The best fit to its spectra includes 2 black body components with $T_1=2.6\times 10^6$ K ($R_1=3.3$ km) and $T_2=5\times 10^6$ K ($R_2=0.75$ km), where R_1 and R_2 are black body radii, without power-law component. The X-ray flux $f(0.5\text{-}10$ keV) $=4.2\times 10^{-12}$ erg/cm²s (XMM, Chandra) and $f(0.1\text{-}2.4$ keV) $=3.4\times 10^{-12}$ erg/cm²s (XMM, Chandra) with a neutral hydrogen column density $N_H=4.5\times 10^{21}$ cm⁻² (XMM, Hui and Becker 2006a).

A statistically significant (possible) period ~ 0.22 s was measured based on XMM observations (Hui and Becker 2006a). No PWN was detected around this neutron star

in XMM and Chandra data. Since there is no PWN, \dot{E} must be less than about 10^{35} erg/s and correspondingly the upper limit on \dot{P} must be about 3×10^{-14} . So, its characteristic age must be at least 10^5 yr, whereas the age of Puppis A (which RX J0822-4300 is connected to) was measured to be only 3000-4000 yr (Hailey and Craig 1995; Brazier et al. 1996; DeLuca et al. 2003). This case is similar to 1E 1207.4-5209 - SNR G296.5+10.0, if the possible period P 0.22 s is confirmed by longer timing observations.

Puppis A is an S-type SNR (Green 2006). It is Oxygen rich that the progenitor might be a very massive star and the SN could probably be type II. Age measurements of show that Puppis A is a young SNR: $t=3400$ yr (Winkler et al. 1988), $t=3700$ yr (Braun et al. 1989; Kaspi et al. 1996; Dechristopher and Winkler 1994; Brazier and Johnston 1999). Puppis A, unlike Vela, is not in the direction of star formation regions and distances of the OB associations in the star formation region located in a nearby direction do not exceed 1.5-1.8 kpc (Melnik and Efremov 1995; Humphreys 1978; Guseinov et al. 2004a). HI clouds in this direction (from 21 cm measurements) are also at $d=1.5-1.8$ kpc (Braun et al. 1989). There are OH clouds in front of the SNR without interacting with it (Woermann et al. 2000). The SNR is out of the HII region it was once in and the eastern part of the SNR is interacting with an HI cloud (Reynoso et al. 1995). So, a possible evolutionary scenario for this SNR is that the progenitor was a very massive star which has partly ionized an HI cloud turning the inner part of it into an HII region in which it has been exploded about 3500-4000 years ago as a type II SN. Initially, the SNR has expanded within the HII cavity (the ionized part of the cloud) and then reached the HI boundary (non-ionized part) of the cloud, presently interacting with it.

The measured values of N_H for Puppis A are $(2-6) \times 10^{21}$ cm^{-2} (Winkler et al. 1981a, 1981b), $(2.9-4.7) \times 10^{21}$ cm^{-2} (Blair et al. 1995; Zavlin et al. 1999).

2.5.4. CXOU J185238.6+004020

This source has recently been identified as an X-ray pulsar with $P=105$ ms and an upper limit on the period change $\dot{P} < 7 \times 10^{-14}$. These values give the lower and upper limits: $\dot{E} < 2 \times 10^{36}$, $B < 3 \times 10^{12}$, $\tau > 24$ kyr. A one-black body with $kT=0.44$ keV ($R=0.9$ km) fits very well to its spectrum. The bolometric X-ray luminosity is $L(\text{bol})=3.7 \times 10^{33}$ erg/s for $d=7.1$ kpc (XMM, Gotthelf et al. 2005).

Halpern et al. (2007) claim that a power-law fit is also good but the corresponding N_H is very large compared to N_H of the SNR. A black body fit with $kT=0.46$ keV gives both a good reduced χ^2 and $N_H=1.4 \times 10^{22}$ cm^{-2} which is comparable to the SNR's N_H . They give the X-ray luminosity $L(\text{bol})=3 \times 10^{33}$ erg/s.

Kes 79 (G33.6+0.1), which is connected to CXOU J185238.6+004020, is an S-type SNR with strong lines of Mg, Si, S. The measured distance values for this SNR are: $d=10$ kpc (21 cm measurements, Frail and Clifton 1989), $d=5.2$ kpc (Σ -D relation, Guseinov et al. 2003c), $d=7$ kpc (Guseinov et al. 2003d). Its neutral hydrogen column density is $N_H=1.6 \times 10^{22}$ cm^{-2} (Sun et al. 2004). A distance of 7 kpc is adapted in this thesis.

Similar to the neutron stars above, there is no PWN around this young neutron star (XMM, Gotthelf et al. 2005) that $\dot{P} < 3 \times 10^{-15}$. So, $\tau > 5 \times 10^5$ yr, but t_{SNR} is only $(6-12) \times 10^3$ yr (Seward et al. 2003).

3. XMM-NEWTON

The information given below are from XMM-Newton website. The XMM-Newton (X-ray Multi-Mirror Mission) is the second of European Space Agency's four cornerstone missions defined in the Horizon 2000 Programme. It was launched on December 10, 1999.

3.1. Spacecraft

3.1.1. Components

The XMM-Newton satellite is configured modularly and is composed of four main elements:

- The Focal Plane Assembly (FPA), consisting of the Focal Plane Platform (FPP) carrying the focal-plane instruments: two Reflection Grating Spectrometer (RGS) readout cameras, an EPIC PN and two EPIC MOS imaging detectors, and the data handling and power distribution units for the cameras. The EPIC and RGS instruments are fitted with radiators, which cool the CCD detectors via cold fingers.
- The Telescope Tube (a long carbon fibre tube), maintaining the relative position between the FPA and the MSP. Due to its length of 6.80 m, the Telescope Tube is physically composed of two halves: the upper and lower tubes. The upper tube includes two reversible venting and outgassing doors (VOD), and supports the outgassing baffle (OGB).
- The Mirror Support Platform (MSP), consisting of the platform itself and carrying the three mirrors assemblies (Mirror Modules + entrance and exit baffles + doors + two RGS grating boxes), the Optical Monitor (OM) and the two star-trackers.
- The Service Module (SVM), which carries the spacecraft subsystems and associated units providing the necessary resources to the satellite. Also attached to the

SVM are the two solar-array wings, the Telescope Sun Shield (TSS) and the two S-band antennas mounted on their booms.

The different components of the XMM spacecraft and its payload are visible in sketch in which XMM has been "dissected", as shown in the following image. The X-ray telescopes, two with Reflection Grating Arrays, are visible at the lower left. At the right end of the assembly, the focal instruments are shown: The EPIC MOS cameras with their radiator, the radiator of the EPIC p-n camera and those of the RGS receivers.

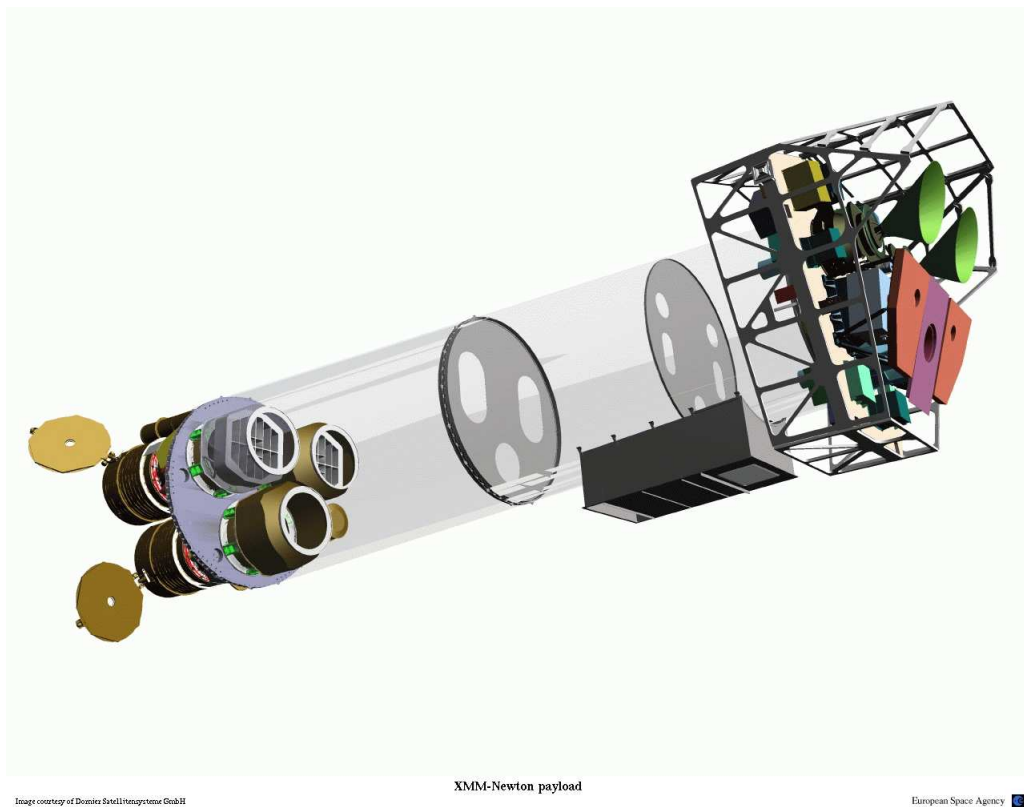


Figure 3.1. If the XMM spacecraft were made of glass, one could gain the above view of its payload. Image courtesy of Dornier Satellitensysteme GmbH / ESA.

3.1.2. Structural Design

The spacecraft structure, like any other structure, is there primarily to guarantee the integrity of the spacecraft under any loading, such as during handling, testing

and launch. In addition, it must allow the spacecraft to serve as an optical bench for a telescope and therefore the structure must provide the necessary thermo-elastic stability in orbit. In the case of XMM-Newton, this led immediately to the selection of ultra-high-modulus carbon-fibre composites (low thermal expansion) for the main structural elements. Another advantage of this material is its very high modulus of elasticity, which limits structural mass for a structure like this, which is (also) designed for stiffness.

These two favourable qualities of this carbon-fibre material, plus its low mass, have led to its widespread use on XMM, albeit for different reasons in different parts. For instance, for the telescope tube and the mirror support platform, a carbon-fibre composite was necessary for thermo-elastic reasons. A strongly directional lay-up made it possible to meet the requirements, whereas the mass could be kept low. On the other hand, for the central cone of the Service Module, the stiffness required was the main reason for using a carbon-fibre composite.

In complex items, such as the mirror support platform, the joints that are necessarily made out of metal degraded the intended high thermo-elastic stability to such a level that active thermal control was necessary. Here, a carbon-fibre composite was selected for its high stiffness and strength. Other parts outside the optical path were made of aluminium for reasons of thermal conductivity (honeycomb for Service Module side panels), light-tightness and ease of production (telescope Sun shield, outgassing baffle).

3.1.3. Thermal constraints

The mirror shells of the Mirror Modules have to be kept at an average temperature of 20°C, with spatial maximum temperature differences of $\pm 2^\circ\text{C}$ in order to limit thermo-elastic deformations. Therefore, the platform is maintained almost isothermal, with deviations of less than $\pm 2^\circ\text{C}$. On the other hand, the Service Module equipment presents quite standard temperature ranges and attention is therefore mainly paid to simplicity and reliability.

The thermal design of XMM takes the full advantage of the stable environment provided by its high-altitude, long-period orbit and by the limited variation of solar attitude angles ($\pm 20^\circ$ pitch combined with $\pm 20^\circ$ roll). In fact, the Earth albedo and infrared heat fluxes are negligible along the largest part of its high-altitude orbit. Only at perigee passes, when the altitude reduces to 7000 km, XMM's thermal stability is slightly affected by the influence of the Earth.

The largest thermal perturbations occur during the eclipse seasons, when the satellite does not receive the Sun's energy for a maximum period of 1.7 h (although, on average, the eclipses are much shorter). However, eclipses always occur below the minimum altitude that is required for observation (40 000 km), leaving time for the spacecraft to recover its temperature stability. Boost heating performed before and after the eclipses by means of heater helps to reduce the time needed for recovery of the temperature drop caused by eclipses.

In order to cope with all orbital perturbations and with changes of satellite attitude, the telescope tube is completely insulated from the external environment and the heater power that is dissipated inside it can be almost continuously adjusted to compensate for changes.

3.2. Mirrors

3.2.1. Introduction

Each of the three X-ray telescopes on board XMM-Newton consists of 58 Wolter I grazing-incidence mirrors which are nested in a coaxial and confocal configuration. The design of the optics was driven by the requirement of obtaining the highest possible effective area over a wide range of energies, with particular emphasis in the region around 7 keV. Thus, the mirror system had to utilize a very shallow grazing angle of $30'$ in order to provide sufficient reflectivity at high energies. The telescopes focal length is 7.5 meters and the diameter of the largest mirrors is 70 cm, to be compatible with the shroud of the launcher. Each telescope consists includes, apart from the mirror

modules, baffles for visible and X-ray stray-light suppression and an electron deflector for diverting soft electrons. Two of the telescopes carry a Reflection Grating Array (RGA).

3.2.2. Telescope Configuration

Each of the XMM-Newton telescopes consists of:

- the mirror assembly door, which protected the optics during integration, launch and early orbit phase,
- the entrance baffle, which provides visible straylight suppression at angles larger than 47° ,
- the X-ray baffle,
- the Mirror Module,
- an electron deflector, which produces a circumferential magnetic field which prevents low energy electrons reflected by the mirrors reaching the focal plane detectors,
- in two of the telescopes, the Reflection Grating Array, and
- the exit baffle, which provides an appropriate thermal environment.

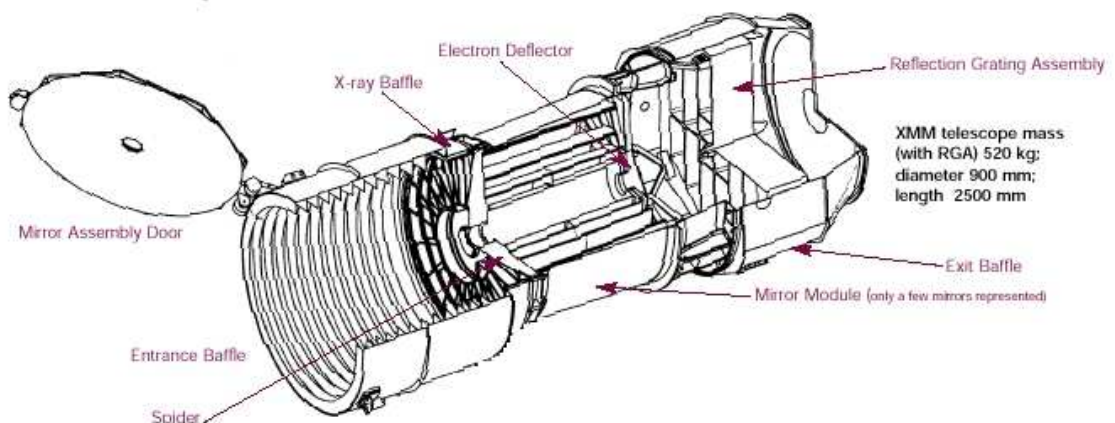


Figure 3.2. Technical drawing of one of the XMM-Newton telescopes. Image courtesy ESA.

The 58 Wolter I mirrors of each telescope are bonded on their entrance aperture to the 16 spokes of a single spider made out of Inconel. The spider is connected to the support platform via an aluminium interface structure (the MIS: Mirror Interface Structure) consisting of an outer cylinder and an interface ring. On two of the modules, the ring interfaces the mirror module to a Reflection Grating Assembly (RGA). To minimise the mechanical deformation of the mirrors and therefore the optical degradation, the flatness of the interface between the spider and the MIS had to be better than 5 micron.

X-ray baffles are located in front of the mirror systems. They act as collimators and reduce considerably the amount of straylight in the field of view of the focal plane cameras.

The XMM-Newton X-ray baffle was constructed as two sieve-plates made out of circular strips. The plates were mounted coaxial to and coaligned with the front aperture cross section of the 58 mirror shells, such that they block single-reflection rays, but do not eclipse two-reflection rays. Each sieve plate is a disk 1 mm thick with 59 circular strips and 16 radial spokes. The offset of the two sieve plates from the front of the mirror system is 385 mm and 439 mm, respectively. All the baffle surfaces facing the mirrors are blackened.

3.2.3. Optical Design

Each Mirror Module is a grazing-incidence Wolter I telescope, consisting of 58 gold-coated nested mirrors. Each mirror shell consists of a paraboloid and an associated hyperboloid which were replicated together in one piece to facilitate alignment and integration.

In grazing incidence optics the effective area is increased by nesting a number of mirrors and thus filling the front aperture as far as possible. The nesting efficiency is determined by the mirror shell thickness and, in case of very low grazing angles, by the minimum radial mirror separation which is required for integration and alignment.

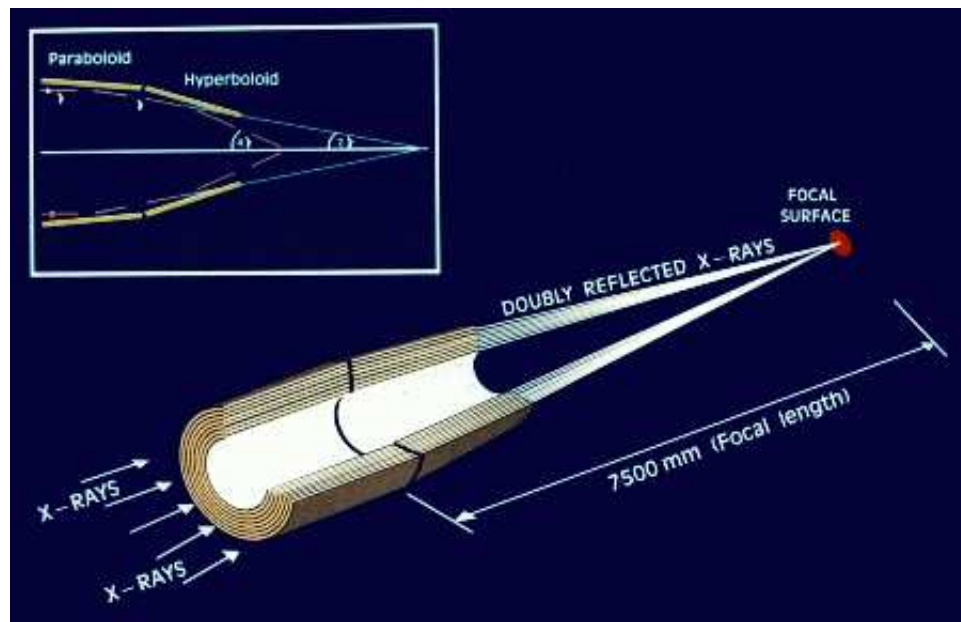


Figure 3.3. Light path in the XMM-Newton telescope with only an EPIC camera in its primary focus (left), and in the two telescopes in which a RGA is mounted into the optical path (right). Image courtesy ESA.

The thinner the mirror shells are and the narrower the shells are spaced, the larger is the collecting area.

The thickness of the smallest mirror (diameter=306 mm) is 0.47 mm, and it increases linearly with shell diameter in order to guarantee sufficient stiffness. The thickness of the 700 mm diameter mirror is 1.07 mm. The minimum radial separation between adjacent shells is 1mm. Adding more shells is rather inefficient in building up more collecting area because of the mass penalty involved and the low gain in effective area.

The performance of the X-ray telescopes can be characterized by:

- the image quality,
- the effective area, and
- the straylight rejection efficiency.

3.2.3.1. Image Quality. The point spread functions and effective areas of the three telescopes were first characterized on-ground during an extensive calibration campaign. A comprehensive numerical model of the mirror system was used to generate an initial calibration database by extrapolating on-ground tests to in-orbit operation conditions and by interpolating between the finite number of measurement points.

On January 19 2000 the X-ray telescope FM2 saw "First Light", followed by FM3 and FM4. After "First Light" a number of observations were made during the commissioning phase in order to characterize the imaging performance of the telescopes. Analysis of the results indicated that the telescopes point responses measured in-orbit were basically the same as derived from on-ground calibration measurements out to 30". In particular, extended sources in the center of the telescope field of view can be studied with a 5" spatial resolution.

For on-axis sources, high energy photons are focused predominantly by the inner shells of the telescope. These inner shells apparently give better focus than the average hence the fractional encircled energy increases with increasing photon energy.

3.2.3.2. Effective Area. The design driver for the XMM-Newton telescopes was to achieve maximal area at low energies (2 keV) without sacrificing area at high energies (7 keV). XMM mirrors are most efficient in the energy range from 0.1 to 10 keV, with a maximum around 1.5 keV and a pronounced edge near 2 keV (the Au M edge). The design goal was to achieve a collecting area of 1900 cm² for energies up to 150 eV, 1500 cm² at 2 keV, 900 cm² at 7 keV, and 350 cm² at 10 keV, for each of the telescopes.

The effective area for each telescope was measured in the PANTER X-ray test facility illuminating the full aperture with line radiation between 0.28 and 10 keV, and using a copy of the ROSAT PSPC as focal plane detector.

3.2.3.3. X-Ray Straylight Rejection. X-rays from outside the field of view can reach the sensitive area of the focal plane detectors by single reflection from the rear end of

the hyperbola, if the source is at an off-axis angle between $20'$ and $80'$. Rays reflected just once from any one of the parabolas cannot leave the mirror assembly because of the close packing of the mirror shells.

The efficiency of the sieve plate system was ray traced and demonstrated to reduce the straylight level by a factor of 5 to 10 depending on the position in the focal plane. Pointings in the vicinity of the Crab Nebula confirmed the high efficiency of the baffles. The straylight collecting area of the EPIC detectors as a function of off-axis angle is about 3 cm^2 for sources located between $20'$ and 1.4° from the optical axis, and completely negligible at higher angles.

3.3. EPIC

3.3.1. Introduction

The XMM-Newton spacecraft is carrying a set of three X-ray CCD cameras, comprising the European Photon Imaging Camera (EPIC). Two of the cameras are MOS (Metal Oxide Semi-conductor) CCD arrays (referred to as the MOS cameras). They are installed behind the X-ray telescopes that are equipped with the gratings of the Reflection Grating Spectrometers (RGS). The gratings divert about half of the telescope incident flux towards the RGS detectors such that (taking structural obscuration into account) about 44 % of the original incoming flux reaches the MOS cameras. The third X-ray telescope has an unobstructed beam; the EPIC instrument at the focus of this telescope uses pn CCDs and is referred to as the pn camera.

The EPIC cameras offer the possibility to perform extremely sensitive imaging observations over the telescope's field of view (FOV) of 30 arcmin and in the energy range from 0.15 to 15 keV with moderate spectral ($E/\Delta E \sim 20-50$) and angular resolution (PSF, 6 arcsec FWHM).

All EPIC CCDs operate in photon counting mode with a fixed, mode dependent frame read-out frequency, producing event lists, i.e. tables with one entry line per

received event, listing (among others) attributes of the events such as the position at which they were registered, their arrival time and their energies. The two types of EPIC, however, differ in some major aspects. This does not only hold for the geometry of the CCD arrays and the instrument design but also for other properties, like e.g., their readout times.

3.3.2. Chip Geometry

Comparison of focal plane organisation of EPIC MOS and pn cameras

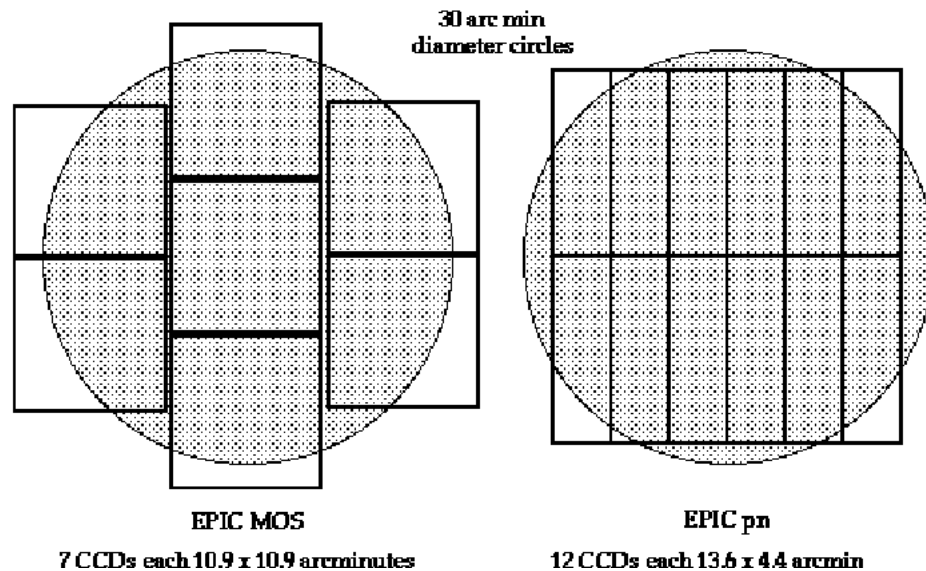


Figure 3.4. A rough sketch of the field of view of the two types of EPIC camera; MOS (left) and pn (right). The shaded circle depicts a diameter area. For the alignment of the different cameras with respect to each other in the XMM-Newton focal plane refer to the text.

3.3.2.1. MOS CCDs. The MOS EEV CCD22 is a three-phase frame transfer device on high resistivity epitaxial silicon with an open-electrode structure; it has a useful quantum efficiency in the energy range 0.2 to 10 keV. The low energy response of the conventional front illuminated CCD is poor below ~ 700 eV because of absorption in the electrode structure. For EPIC MOS, one of the three electrodes has been enlarged to occupy a greater fraction of each pixel, and holes have been etched through this enlarged electrode to the gate oxide. This gives an "open" fraction of the total pixel

area of 40 %; this region has a high transmission for very soft X-rays that would have otherwise be absorbed in the electrodes. In the etched areas, the surface potential is pinned to the substrate potential by means of "pinning implant". High energy efficiency is defined by the resistivity of the epitaxial silicon (around 400 Ohm-cm). The epitaxial layer is 80 microns thick (p-type). The actual mean depletion of the flight CCDs is between 35 to 40 microns: the open phase region is not fully depleted.

3.3.2.2. PN CCDs. The schematic view looking into the pn-CCD introduces intuitively the advantages of the concept: X-rays hit the detector from the rear side. In the event of an X-ray interaction with the silicon atoms, electrons and holes are generated in numbers proportional to the energy of the incident photon. The average energy required to form an electron-hole pair is 3.7 eV at -90° C. The strong electric fields in the pn-CCD detector separate the electrons and holes before they recombine. Signal charges (in our case electrons), are drifted to the potential minimum and stored under the transfer registers. The positively charged holes move to the negatively biased back side, where they are 'absorbed'. The electrons, captured in the potential wells 10 microns below the surface can be transferred towards the readout nodes upon command, conserving the local charge distribution patterns from the ionization process. Each CCD line is terminated by a readout amplifier.

3.3.3. Operating Modes

The EPIC cameras allow several modes of data acquisition. Note that in the case of MOS the outer ring of 6 CCDs remain in standard full-frame imaging mode while the central MOS CCD can be operated separately. The pn camera CCDs can be operated in common modes in all quadrants for full frame, extended full frame and large window mode, or just with one single CCD (CCD0 in quadrant 1) for small window, timing and burst mode.

1. Full frame and extended full frame (pn only); in this mode, all pixels of all CCDs are read out and thus the full FoV is covered.
2. Partial window:

a) For MOS; in a partial window mode the central CCD of both MOS cameras can be operated in a different mode of science data acquisition, reading out only part of the CCD chip: in small window mode an area of 100 x 100 pixels is read out, whereas in large window mode an area of 300 x 300 pixels is active.

b) For PN; in large window mode only half the area of all 12 CCDs is read out, whereas in small window mode only the part of CCD0 in quadrant 1 at the focal point is used to collect data.

3. Timing:

a) MOS + PN; in timing mode, imaging is made only in one dimension, along the column axis. Along the row direction, data from a predefined area on one CCD chip are collapsed into a one-dimensional row to be read out at high speed.

b) PN only; a special flavour of the timing mode of the EPIC pn camera is the burst mode, which offers very high time resolution, but has a low duty cycle of 3 %.

3.3.4. Instrument Characteristics

3.3.4.1. Quantum Efficiency. One of the factors to be taken into account when determining the effective area of the EPIC cameras is their quantum efficiency. It is the quantum efficiency of the EPIC-MOS chips that limits the energy passband at its high energy end, while the pn camera can detect photons with high efficiency up to 15 keV.

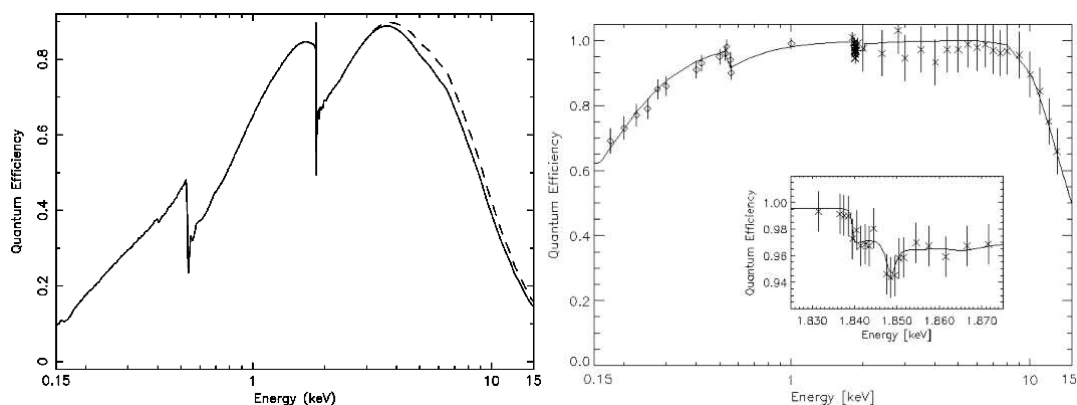


Figure 3.5. Quantum efficiency of the EPIC MOS1 (solid line) and MOS2 (dashed line) CCD1 chip as a function of photon energy. Quantum efficiency of the EPIC pn CCD chips as a function of photon energy (Struder et al., 2001).

3.3.4.2. Background. The EPIC background can be divided into two parts: a cosmic X-ray background (CXB), and an instrumental background. The latter component may be further divided into a detector noise component, which becomes important at low energies (below 200 eV) and a second component which is due to the interaction of particles with the structure surrounding the detectors and the detectors themselves. This component is characterized by a flat spectrum and is particularly important at high energies (above a few keV). The particle induced background can be divided into two components: an external 'flaring' component, characterized by strong and rapid variability, which is often totally absent and a second more stable internal component. The flaring component is currently attributed to soft protons (with energies smaller than a few 100 keV), which are funneled towards the detectors by the X-ray mirrors. The stable component is due to the interaction of high energy particles (with energies larger than some 100 MeV) with the structure surrounding the detectors and possibly the detectors themselves.

Plot of file m1_light_curve.fits

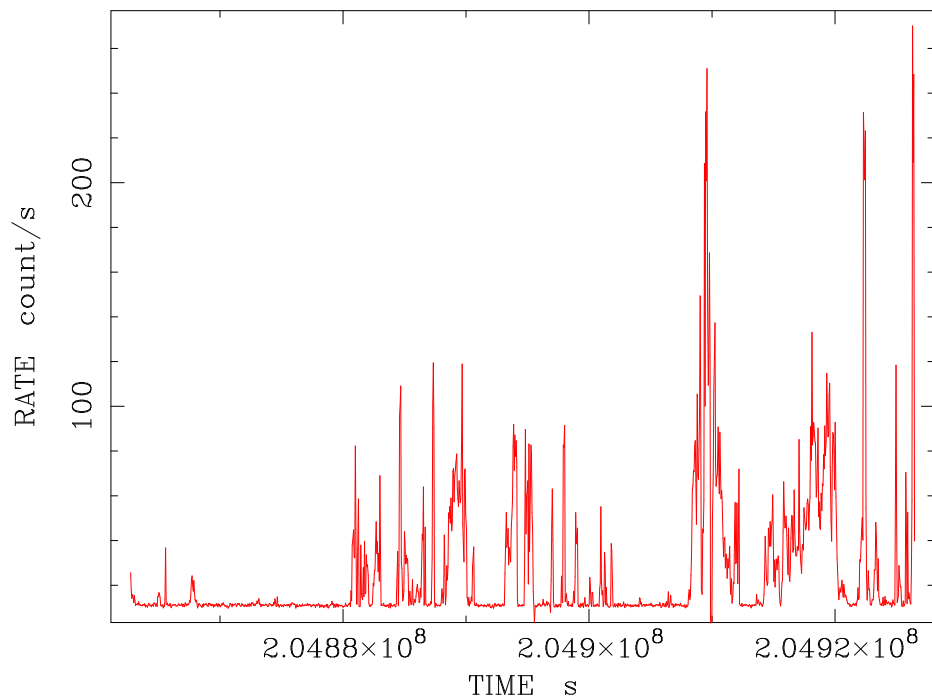


Figure 3.6. Example of light curve from a MOS1 observation badly effected by proton flares.

3.3.5. Filters and Effective Area

As the EPIC detectors are not only sensitive to X-ray photons but also to IR, visible and UV light, the cameras include aluminised optical blocking filters to reduce the contamination of the X-ray signal by those photons.

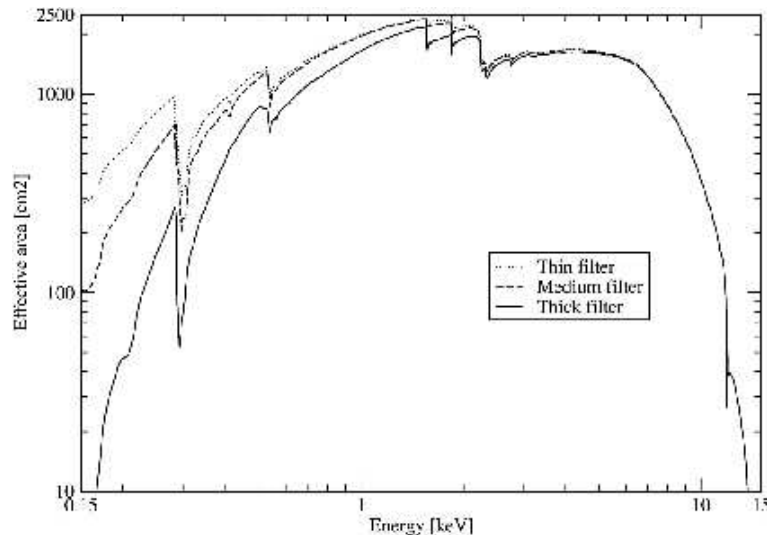


Figure 3.7. Combined effective area of all telescopes assuming that all cameras operate with the same filters, either open, thin, medium or thick.

If such photons are registered by the EPIC detectors, the data analysis would be impeded in three ways:

1. Shot noise on the optically generated photo-electrons will increase the overall system noise
2. The energy scale will be incorrectly registered, because a nominally zero signal will have a finite offset. For each optically generated photo electron, the energy scale shifts by about 3.6 eV.
3. Optically-generated photo electrons can lead to a saturation of electron traps, changing (improving) the charge transfer inefficiency.

There are four filters in each EPIC camera. Two are thin filters made of 1600 Å of poly-imide film with 400 Å of aluminium evaporated on to one side; one is the medium filter made of the same material but with 800 Å of aluminium deposited on

it; and one is the thick filter. This is made of 3300 Å thick Polypropylene with 1100 Å of aluminium and 450 Å of tin evaporated on the film. The filters are self-supporting and 76 mm in diameter. The remaining two positions on the filter wheel are occupied by the closed (1.05 mm of aluminium) and open positions, respectively. The former is used to protect the CCDs from soft protons in orbit, while the open position could in principle be used for observations where the light flux is very low, and no filter is needed.

3.4. RGS

The XMM-Newton payload comprises three co-aligned high throughput telescopes with a FOV of 30 arcmin and spatial resolution of about 6 arcsec (FWHM). Imaging CCD detectors are placed in the focus of each telescope. Behind two of the three telescopes, about half of the X-ray light is utilized by the Reflection Grating Spectrometers (RGS). Each RGS consists of an array of reflection gratings which diffracts the X-rays to an array of dedicated charge coupled devices (CCD) detectors. The RGS instruments achieve high resolving power (150 to 800) over a range from 5 to 35 Å [0.33 to 2.5 keV] (in the first spectral order). The effective area peaks around 15 Å [0.83 keV] (first order) at about 150 cm² for the two spectrometers.

3.4.1. Instrument Design

The RGS design incorporates an array of reflection gratings placed in the converging beam at the exit from the X-ray telescope. The grating stack intercepts roughly half of the X-ray light and deflects it to a strip of CCD detectors offset from the telescope focal plane. The undeflected light passes through and is intercepted by EPIC-MOS in the telescope focal plane. Nine large format back-illuminated CCDs are operated in single photon counting and frame transfer mode at a temperature of -80° C. For each photon, the position and the energy is measured: the position to determine the high resolution X-ray spectrum as diffracted by the grating module, and the energy and position to separate the contributions from the various overlapping grating orders (and from the in-flight calibration source) and to reduce the background.

erage between 170 nm and 650 nm of the central 17 arc minute square region of the X-ray field of view, permitting routine multiwavelength observations of XMM targets simultaneously in the X-ray and ultraviolet/optical bands.

The XMM-OM consists of a Telescope Module and a separate Digital Electronics Module, of which there are two identical units for redundancy. The Telescope Module contains the telescope optics and detectors, the detector processing electronics and power supply. There are two distinct detector chains, again for redundancy. The Digital Electronics Module houses the Instrument Control Unit, which handles communications with the spacecraft and commanding of the instrument, and the Data Processing Unit, which pre-processes the data from the instrument before it is telemetered to the ground.

The Telescope Module consists of a modified 30 cm Ritchey-Chretien telescope with a focal ratio of $f/12.7$, i.e. a focal length of ca. 3.8 m. The incoming light is reflected by a mirror inclined at an angle of 45° to one of two redundant detectors. The OM telescope tube is ca. 2 m long. Incoming light falls onto the primary mirror, which reflects it onto the secondary, from where it goes to the inclined mirror that reflects it onto the detector. A filter wheel is mounted immediately in front of the detectors. This does not only contain filters, but also other optical elements, like gratings and a magnifier (i.e. optics for a longer focal length and thus higher resolution on the sky).

4. OBSERVATION AND DATA REDUCTION

4.1. Observations

X-ray data of isolated radio-quiet neutron stars were obtained by XMM-Newton observations with European Photon Imaging Camera (EPIC) instruments, which consist of the EPIC PN CCD detector (Strueder et al. 2001) and the two EPIC MOS CCD detectors (Turner et al. 2001).

1E 1207.4-5209 was observed with XMM-Newton on 2002 August 4-7 for two time intervals 128 and 130 ks respectively. The PN camera was operated with a thin filter in small-window mode and two MOS cameras were operated with a thin filter in full frame mode.

RX J0002+6246 was observed with XMM-Newton on 2001 August 22-23 for 32 ks. The PN camera was operated with a medium filter in small-window mode and two MOS cameras were operated with a medium filter in full frame mode.

RX J0822-4300 was observed with XMM-Newton on 15 April and 11 August 2001 for 28.8 and 24.3 ks respectively. The PN camera was operated with a thin filter in small-window mode and two MOS cameras were operated with a medium filter in full frame mode.

CXOUJ185238.6+004020 was observed with XMM-Newton on 10 August 2001 for two time intervals 31.4 ks each. The PN camera was operated with a medium filter in small-window mode and two MOS cameras were operated with a medium filter in full frame mode. Table 4.1 gives summary of the observations.

Table 4.1. Log of observations.

Source	OBS-ID	Start Date	Instrument	Instrument Mode	Filter	Time ^a (ks)	Time ^b (ks)
1E 1207.4-5209	0155960301	2002-08-04	PN	P.SmallWindow	Thin	128.2	76.3
1E 1207.4-5209	0155960301	2002-08-04	MOS1	P.FullWindow	Thin	127.6	104.5
1E 1207.4-5209	0155960301	2002-08-04	MOS2	P.FullWindow	Thin	127.5	104.7
1E 1207.4-5209	0155960501	2002-08-06	PN	P.SmallWindow	Thin	129.5	72.9
1E 1207.4-5209	0155960501	2002-08-06	MOS1	P.FullWindow	Thin	129.4	100.3
1E 1207.4-5209	0155960501	2002-08-06	MOS2	P.FullWindow	Thin	129.4	100.2
RX J0002+6246	0016140101	2001-08-22	PN	P.SmallWindow	Medium	32.2	18.0
RX J0002+6246	0016140101	2001-08-22	MOS 1	P.FullWindow	Medium	33.0	14.0
RX J0002+6246	0016140101	2001-08-22	MOS 2	P.FullWindow	Medium	33.0	14.5
RX J0822-4300	0113020101	2001-15-04	PN	P.SmallWindow	Thin	24.2	14.8
RX J0822-4300	0113020101	2001-15-04	MOS 1	P.FullWindow	Medium	22.7	16.4
RX J0822-4300	0113020101	2001-15-04	MOS 2	P.FullWindow	Medium	22.7	17.5
RX J0822-4300	0113020301	2001-11-08	PN	P.SmallWindow	Thin	22.9	15.9
CXOUJ185238.6+004020	0204970201	2004-10-18	PN	P.SmallWindow	Medium	31.0	21.4
CXOUJ185238.6+004020	0204970201	2004-10-18	MOS1	P.FullWindow	Medium	31.2	30.5
CXOUJ185238.6+004020	0204970201	2004-10-18	MOS2	P.FullWindow	Medium	31.2	30.6
CXOUJ185238.6+004020	0204970301	2004-10-23	PN	P.SmallWindow	Medium	31.0	21.6
CXOUJ185238.6+004020	0204970301	2004-10-23	MOS1	P.FullWindow	Medium	31.2	30.2
CXOUJ185238.6+004020	0204970301	2004-10-23	MOS2	P.FullWindow	Medium	31.2	30.3

^aLive Time^bNet Exposure Time

4.2. Data Reduction

The Observation Data Files (ODF) were processed with the XMM-Newton Science Analysis Software (SAS) version 7.0.0. Epic calibrated event lists were generated by the tasks *emchain* and *epchain*. Filtering event list data and creating data products including images, spectra and rate curves were all accomplished using the *evselect* task.

Evselect task supports selections based on intrinsic event attributes falling into the following sub-categories (XMM-Newton USG 4.0, Loiseau, N. et al., 2006):

- (i) Spatial selections for particularly interested regions in any spatial coordinate system,
- (ii) Energy selections for the interested interval in either PHA or PI space,
- (iii) Time selections for the interested interval or Good Time Intervals (GTI),
- (iv) Event selections based on any event properties (e.g PATTERN, CCDNR).

Observations were affected by soft protons flares, so contaminated periods were cleaned. To achieve this, a rate curve of the TIME column in the calibrated event lists were extracted using only high energy (greater than 10keV). Time bin size was chosen 50 sec for rate curve accumulation. The rate curves are examined and the mean values are defined with Gaussians. All time bins out of ± 2.7 (90%) range of the mean count rate which defined the selection of Good Time Intervals (GTI) for each camera were excluded. The mean count rate and ± 2.7 (90%) values are tabulated in Table 4.2.

Table 4.2. The mean count rate values of each observation and 2.7σ (90%) values.

Source	Obs. ID.	PN	MOS1	MOS2
1E 1207.4-5209	0155960301	1.1163 \pm 6.6169	7.6947 \pm 7.3432	8.1568 \pm 7.3788
1E 1207.4-5209	0155960501	1.5491 \pm 5.1314	7.8761 \pm 7.5041	8.1878 \pm 7.8019
RX J0002+6246	0016140101	9.8844 \pm 18.1489	9.6506 \pm 9.1260	9.7694 \pm 9.9746
RX J0822-4300	0113020101	1.6653 \pm 3.8389	6.8513 \pm 9.1816	6.8837 \pm 7.7120
RX J0822-4300	0113020301	0.9889 \pm 6.7559	4.3852 \pm 36.6174	8.5689 \pm 21.4534
CXOUJ185238.6+004020	0204970201	1.4007 \pm 4.7677	10.1340 \pm 7.9547	10.2920 \pm 8.1278
CXOUJ185238.6+004020	0204970301	1.9239 \pm 4.3629	10.6620 \pm 8.8965	10.8220 \pm 8.7588

After removing high particle background intervals, the net exposure times are 76.34 ks and 72.89 ks (PN), 104.5 ks and 100.3 ks (MOS1), 104.7 ks and 100.2 ks (MOS2) for 1E 1207.4-5209 with observations 0155960301 and 0155960501, respectively. Figure 4.1 shows PN, MOS1 and MOS2 light curves of 1E 1207.4-5209. The bin width is 50 sec. Black solid lines represents the average count rate values and dashed lines define $\pm 2.7 \sigma$ levels from the mean value during the quiescent periods.

The net exposure times for RX J0002+6246 are 18.0 ks (PN), 14.0 ks (MOS1), and 14.5 ks (MOS2). During the observations of RX J0002+6246, the detections were strongly effected by soft proton flaring that the net exposure times were shortened more than usual. Figure 4.2 shows PN, MOS1 and MOS2 light curves of RX J0002+6246. The bin width is 50 sec. Black solid lines represents the average count rate values and dashed lines define $\pm 2.7 \sigma$ levels from the mean value during the quiescent periods.

For RX J0822-4300, the net exposure times are 14.8 ks and 15.9 (PN), 16.4 ks (MOS1), and 17.5 ks (MOS2) for the observations 0113020101 and 0113020301 respectively. Figure 4.3 shows PN, MOS1 and MOS2 light curves of RX J0822-4300. The bin width is 50 sec. Black solid lines represents the average count rate values and dashed lines define $\pm 2.7 \sigma$ levels from the mean value during the quiescent periods.

For CXOUJ185238.6+004020, the net exposure times are 21.4 ks and 21.6 ks (PN), 30.5 ks and 30.2 ks (MOS1), and 30.6 ks and 30.3 ks (MOS2) for the observations 0204970201 and 0204970301 respectively. Figure 4.4 shows PN, MOS1 and MOS2 light curves of CXOUJ185238.6+004020. The bin width is 50 sec. Black solid lines represents the average count rate values and dashed lines define $\pm 2.7 \sigma$ levels from the mean value during the quiescent periods.

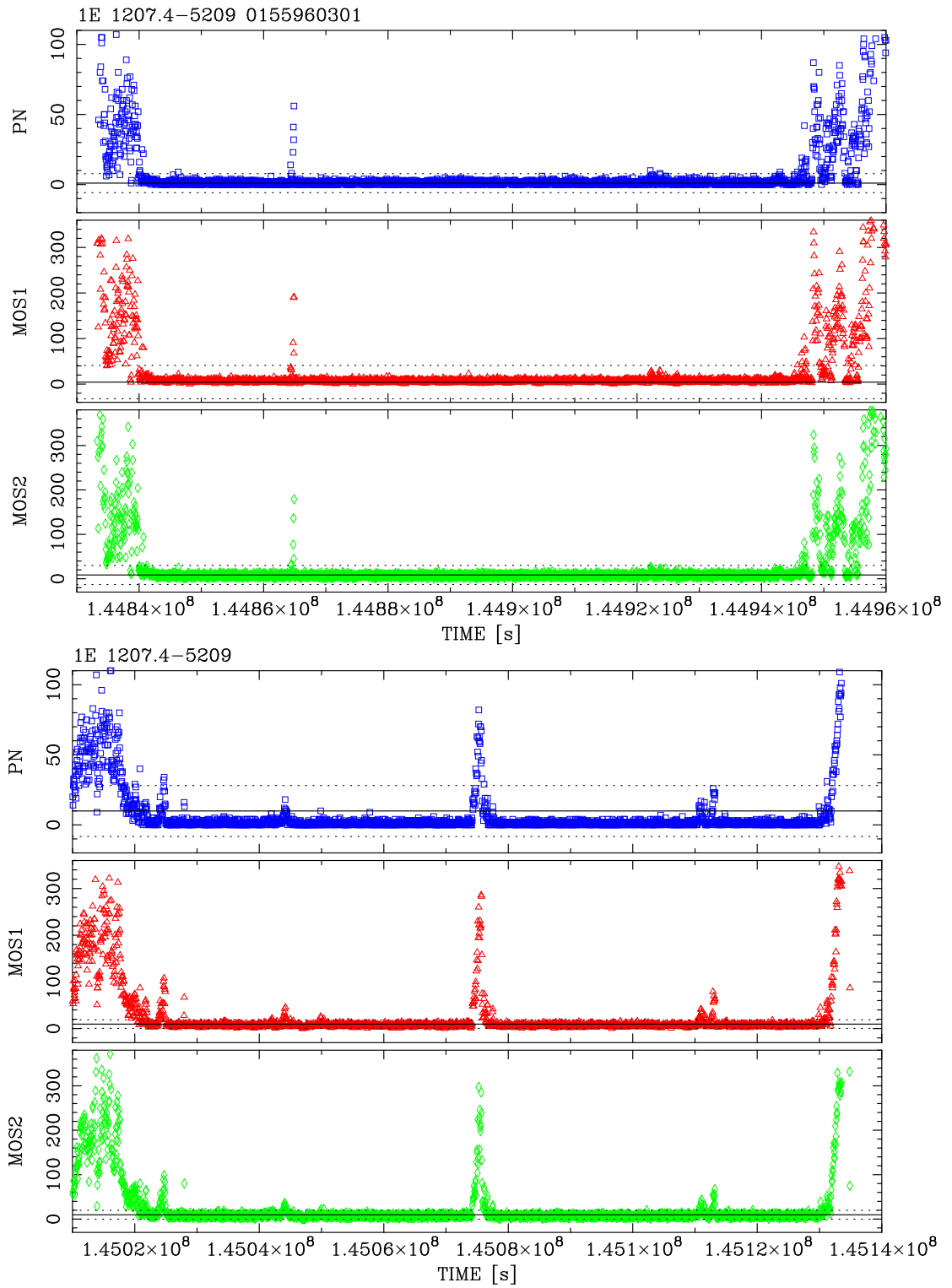


Figure 4.1. PN, MOS1 and MOS2 light curves of 1E 1207.4-5209 with observations 0155960301 (top panel) and 0155960501 (bottom panel).

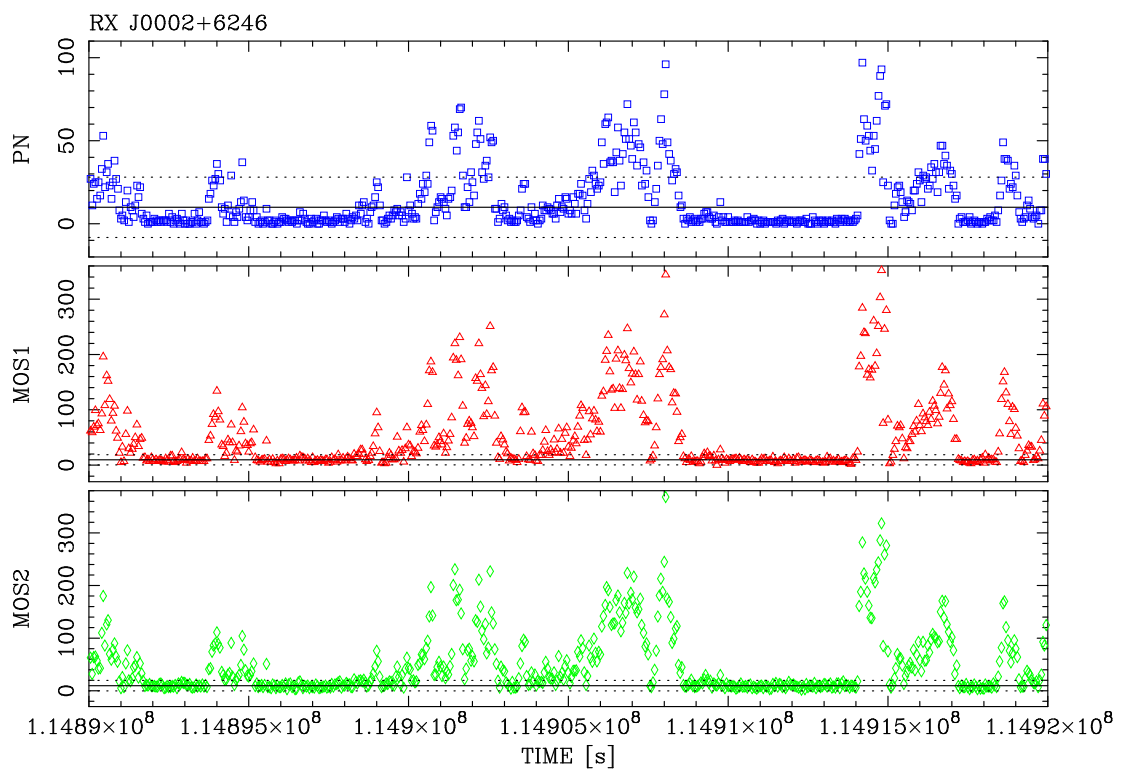


Figure 4.2. PN, MOS1 and MOS2 light curves of RX J0002+6246.

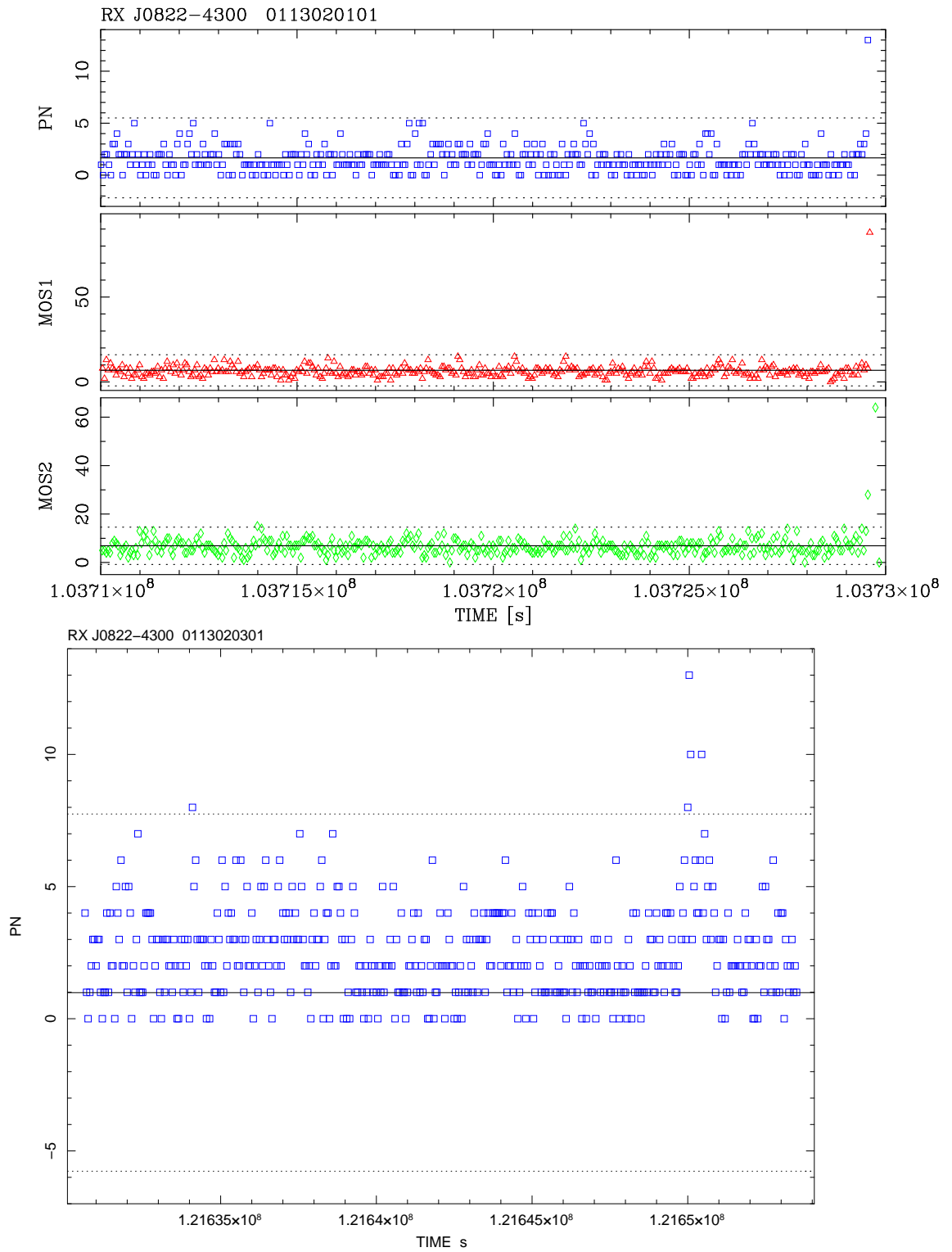


Figure 4.3. PN, MOS1 and MOS2 light curves of RX J0822-4300 with observations 0113020101 (top panel) and 0113020301 (bottom panel).

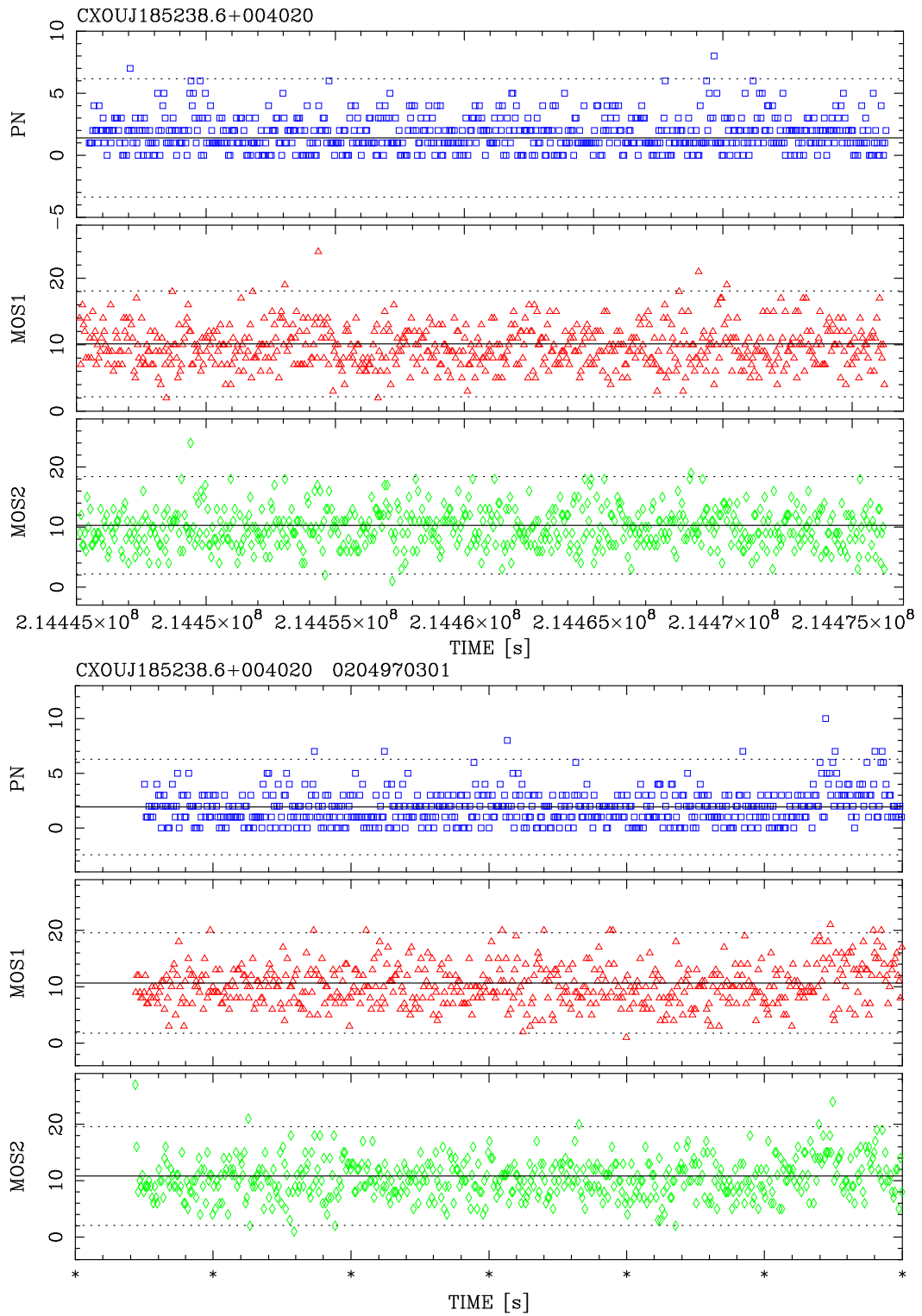


Figure 4.4. PN, MOS1 and MOS2 light curves of CXOUJ185238.6+004020 with observations 0204970201 (top panel) and 0204970301 (bottom panel).

Pile-up effects occur when two or more X-ray photons deposit charge packets in a single pixel as photon pile-up or in neighboring pixels as pattern pile-up, during one read-out cycle. This is a non-negligible possibility when the source is very bright. In such a case these events are recognized as one single event having the sum of their energies. If this happens sufficiently often it will result in a hardening of the spectrum as piled-up soft events are shifted in the spectrum to higher energies (XMM-Newton USG 4.0, Loiseau, N. et al., 2006).

Pile up was checked using the SAS task *epatplot*. Except 1E 1207.4-5209 observations, source count rates were too low for pile-up effects to be significant. For the case of 1E 1207.4-5209, pattern distributions are in agreement with the model curves, pile-up is not a problem. Thus, the events were selected as all valid events (PATTERN ≤ 12) for MOS1 and MOS2, and single and double events (PATTERN in [1:4]) for PN.

4.3. Background Treatment

Background regions were selected according to recommendations of XMM-Newton calibration team (EPIC status of calibration and data analysis Kirsch, M., 2006) from the same observation and the same CCD. To avoid out-of-time events from the source, circular region was preferred to annulus around the source region. ‘FLAG == 0’ used to screen PN event files to exclude the events next to edges of the CCDs and next to bad pixels.

The fraction of Out-of-Time (Oot) events scales with the mode-dependent ratio of integration and readout time and is not high for the PN Small Window mode 1.1% and MOS Full Frame Mode 0.35%. (XMM-Newton UHB 2.4, Ehle, M. et al., 2006) Also there doesn’t seem any Oot events overlap the sources being investigated, so Oot correction wasn’t applied.

For 1E 1207.4-5209, source and background region was extracted from a 45” radius circle for all cameras (see Figure 4.5, Figure 4.6, Figure 4.7, Figure 4.8, Figure 4.9, Figure 4.10).

For RX J0002+6246, source and background region was extracted from a 13'' radius circle for all cameras (see Figure 4.11, Figure 4.12, Figure 4.13).

For RX J0822-4300, source and background region was extracted from a 18'' radius circle for all cameras (see Figure 4.14, Figure 4.15, Figure 4.16, Figure 4.17).

For CXOUJ185238.6+004020, source and background region was extracted from a 15'' radius circle for all cameras (see Figure 4.18, Figure 4.19, Figure 4.20, Figure 4.21, Figure 4.22, Figure 4.23).

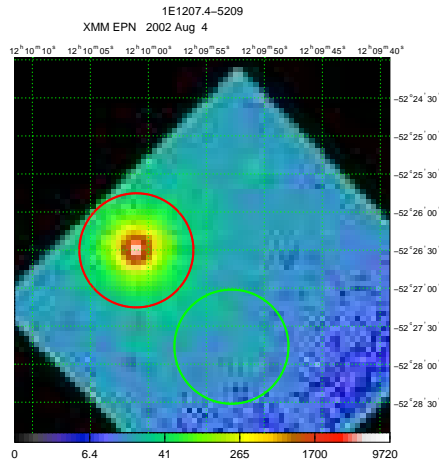


Figure 4.5. EPIC PN image of 1E 1207.4-5209 obs. 0155960301.

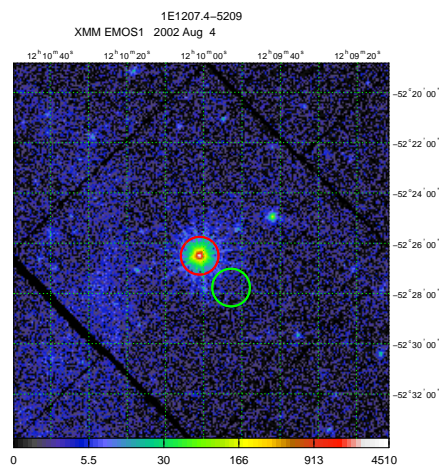


Figure 4.6. EPIC MOS1 image of 1E 1207.4-5209 obs. 0155960301.

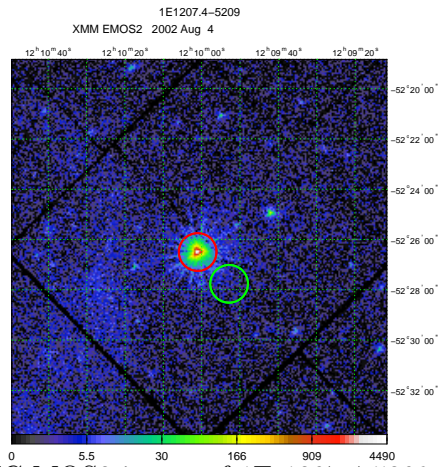


Figure 4.7. EPIC MOS2 image of 1E 1207.4-5209 obs. 0155960301.

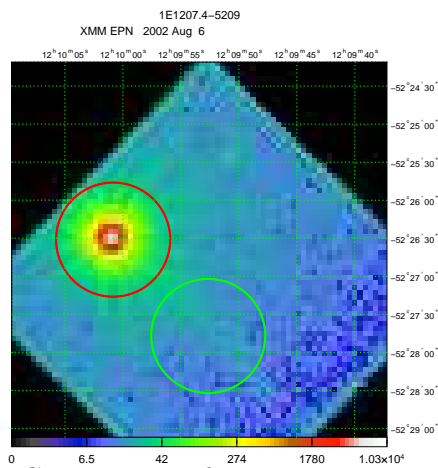


Figure 4.8. EPIC PN image of 1E 1207.4-5209 obs. 0155960501.

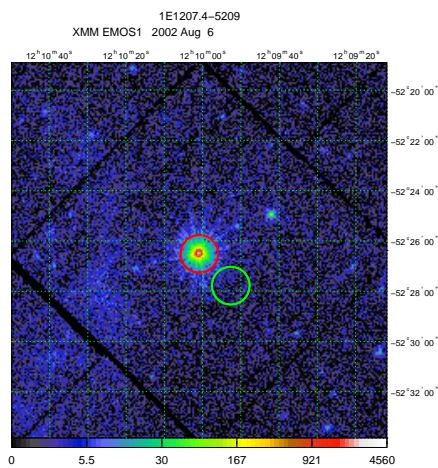


Figure 4.9. EPIC MOS1 image of 1E 1207.4-5209 obs. 0155960501.

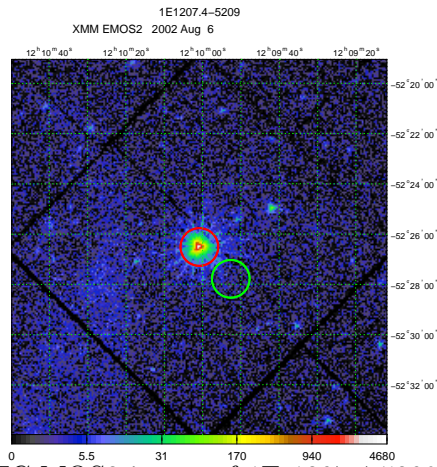


Figure 4.10. EPIC MOS2 image of 1E 1207.4-5209 obs. 0155960501.

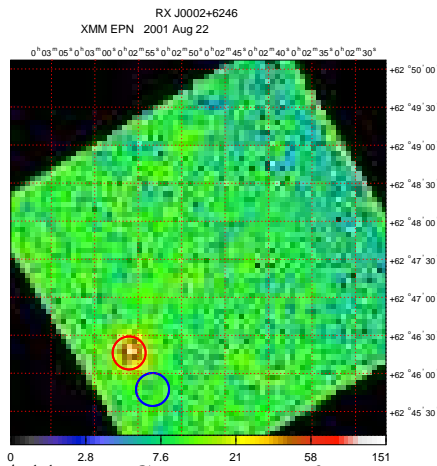


Figure 4.11. EPIC PN image of RX J0002+6246.

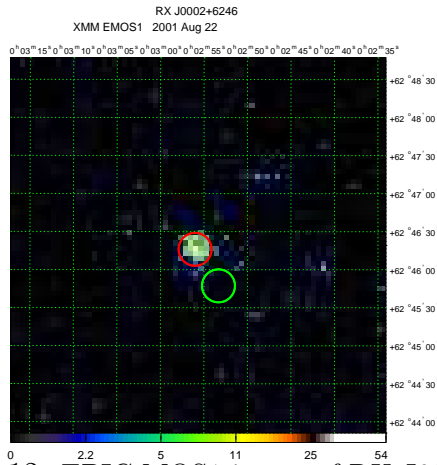


Figure 4.12. EPIC MOS1 image of RX J0002+6246.

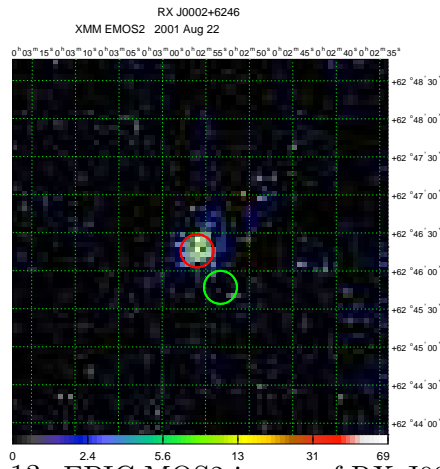


Figure 4.13. EPIC MOS2 image of RX J0002+6246.

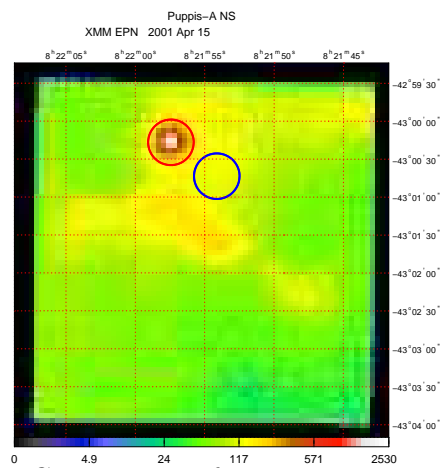


Figure 4.14. EPIC PN image of RX J0822-4300 obs. 0113020101.

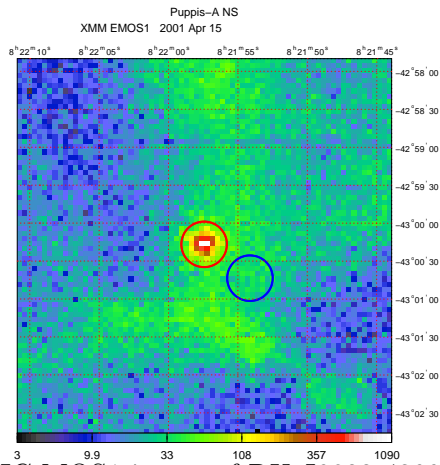


Figure 4.15. EPIC MOS1 image of RX J0822-4300 obs. 0113020101.

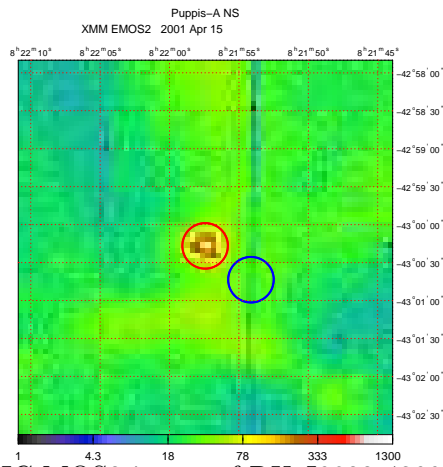


Figure 4.16. EPIC MOS2 image of RX J0822-4300 obs. 0113020101.

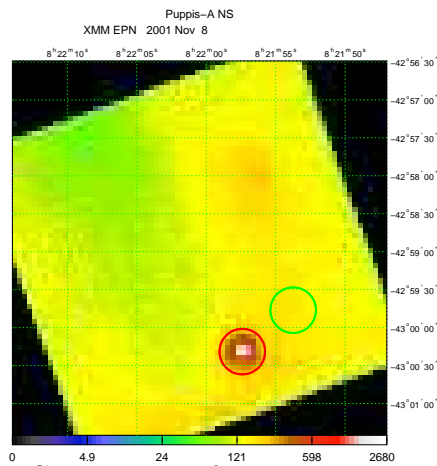


Figure 4.17. EPIC PN image of RX J0822-4300 obs. 0113020301.

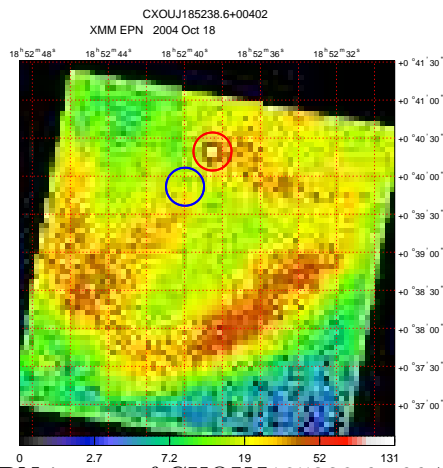


Figure 4.18. EPIC PN image of CXOUJ185238.6+004020 obs. 0204970201.

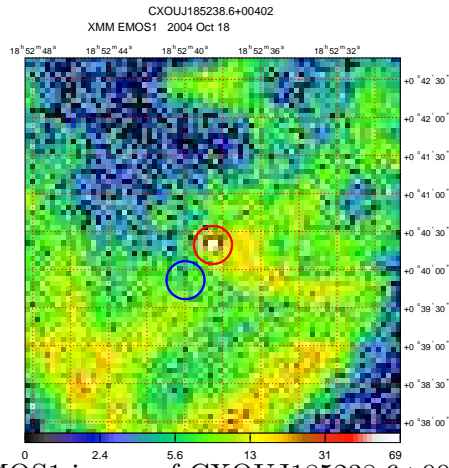


Figure 4.19. EPIC MOS1 image of CXOUJ185238.6+004020 obs. 0204970201.

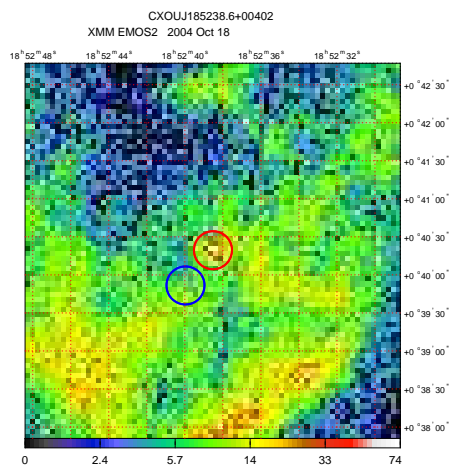


Figure 4.20. EPIC MOS2 image of CXOUJ185238.6+004020 obs. 0204970201.

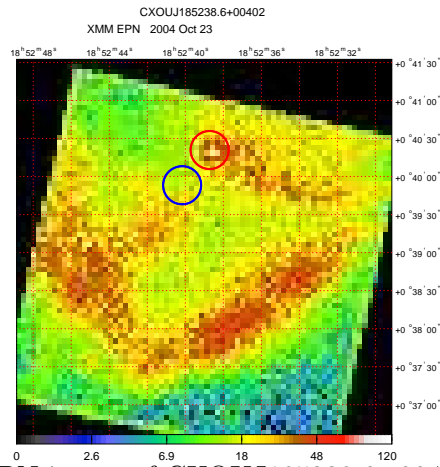


Figure 4.21. EPIC PN image of CXOUJ185238.6+004020 obs. 0204970301.

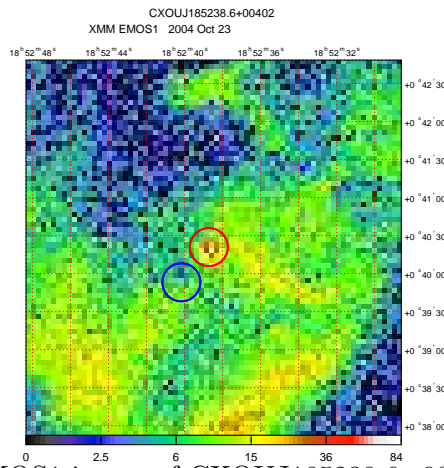


Figure 4.22. EPIC MOS1 image of CXOUJ185238.6+004020 obs. 0204970301.

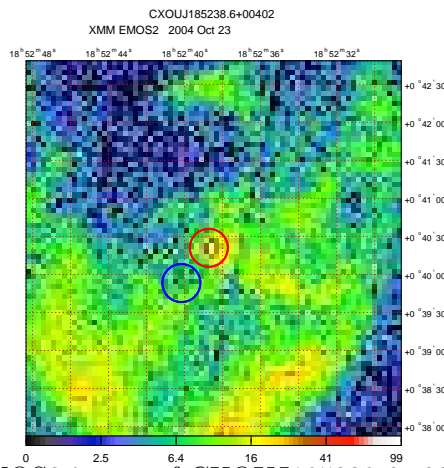


Figure 4.23. EPIC MOS2 image of CXOUJ185238.6+004020 obs. 0204970301.

5. ANALYSIS AND RESULTS

Source and background spectra were generated separately via the *evselect* task. Spectrum of PI channels were created by the standard selections as single and double events (PATTERN in [1:4]), 'FLAG == 0', spectral binsize 5, spectral channel range between 0 and 20479 for PN and all valid events (PATTERN \leq 12), #XMMEA_EM flag, spectral binsize 15, spectral channel range 0-11999 for MOS1/2 in the energy range 0.3-10.0 keV. Response matrices and ancillary files were generated by the SAS task *rmfgen* and *arfgn*.

The spectral analysis was performed by XSPEC 7.0. Black body (bb), power law (pow), gaussian absorption lines (gabs) and photo-electric absorption (wabs) models were used (XSPEC User's Guide 12.2.1, Arnaud, K. et al., 2006).

Photo-electric absorption using Wisconsin cross-sections is defined as $M(E) = \exp(-N_H\sigma(E))$ where N_H is the equivalent hydrogen column density (in units of 10^{22} atoms cm^{-2}) and $\sigma(E)$ is the photo-electric cross-section (not including Thomson scattering, this model uses the Anders and Ebihara relative abundances).

Black body spectrum is defined as $A(E) = \frac{K \times 8.0525 E^2 dE}{kT^4 [\exp(E/kT) - 1]}$ where kT is the temperature in keV and K is the ratio L_{39}/D_{10}^2 where L_{39} is the source luminosity in units of 10^{39} ergs $^{-1}$ and D_{10} is the distance to the source in units of 10 kpc.

Gaussian absorption line is defined as $M(E) = \exp(-(\tau_{opt}/\sqrt{2\pi}/w) \exp(-.5((E-E_0)/w)^2))$ where E_0 is the line energy in keV, w is the line width in keV and τ_{opt} is the optical depth.

Simple photon power law spectrum is defined as $A(E) = KE^{-\alpha_p}$ where α_p is the photon index of the power law and K is the number of photons $\text{keV}^{-1} \text{cm}^{-2} \text{s}^{-1}$ at 1 keV.

5.1. 1E 1207.4-5209

The results of PN, MOS1 and MOS2 data are represented in Table 5.1. The spectra were rebinned by *grppha* in order to have at least 40 counts per bin. The energy range was chosen to be 0.3-4.0 keV as the source is marginally detected beyond 4 keV. Single component black body or power law does not fit the data well. Two black body or black body plus power law fits give relatively better results, but still the reduced χ^2 values are too high. The best fit includes two black body components with three Gaussian absorption lines (see Figure 5.1, Figure 5.2, Figure 5.3) (reduced $\chi^2=1.16$ for 784 degrees of freedom). The black body temperatures are 0.15 and 0.3 keV with $N_H=1\times 10^{21}$ cm^{-2} which is comparable to the SNR's N_H . The luminosity of 1E 1207.4-5209 is 2×10^{33} erg/s for $d=2$ kpc.

Table 5.1. Spectral parameters of 1E 1207.4-5209.

Parameter	PN	MOS1	MOS2
N_H (10^{22} cm^{-2})	$0.097^{+0.001}_{-0.002}$	$0.113^{+0.003}_{-0.002}$	$0.098^{+0.002}_{-0.002}$
kT_{BB1} (keV)	$0.151^{+0.001}_{-0.001}$	$0.166^{+0.252}_{-0.002}$	$0.160^{+0.001}_{-0.001}$
kT_{BB2} (keV)	$0.301^{+0.002}_{-0.002}$	$0.321^{+0.002}_{-0.002}$	$0.313^{+0.002}_{-0.002}$
E_1	$0.681^{+0.002}_{-0.004}$	$0.750^{+0.006}_{-0.004}$	$0.729^{+0.004}_{-0.006}$
τ_1	119^{+1}_{-3}	52^{+1}_{-2}	48^{+1}_{-2}
FWHM_1 (keV)	$0.199^{+0.003}_{-0.002}$	$0.155^{+0.004}_{-0.005}$	$0.154^{+0.005}_{-0.004}$
E_2	$1.398^{+0.006}_{-0.006}$	$1.433^{+0.010}_{-0.008}$	$1.413^{+0.007}_{-0.009}$
τ_2	29^{+2}_{-1}	17^{+1}_{-2}	14^{+1}_{-1}
FWHM_2 (keV)	$0.097^{+0.005}_{-0.005}$	$0.087^{+0.006}_{-0.012}$	$0.072^{+0.007}_{-0.009}$
E_3	$2.258^{+0.015}_{-0.017}$	$2.139^{+0.031}_{-0.060}$	$2.148^{+0.035}_{-0.039}$
τ_3	12^{+4}_{-2}	8^{+4}_{-2}	10^{+3}_{-3}
FWHM_3 (keV)	$0.096^{+0.022}_{-0.013}$	$0.080^{+0.068}_{-0.036}$	$0.082^{+0.049}_{-0.045}$
$flux(\text{ergscm}^{-2}\text{s}^{-1})(0.3\text{-}4.0\text{ keV})$	2.12×10^{-12}	2.11×10^{-12}	2.20×10^{-12}
Reduced chi-squared	1.16	1.52	1.38
D.O.F.	784	274	272

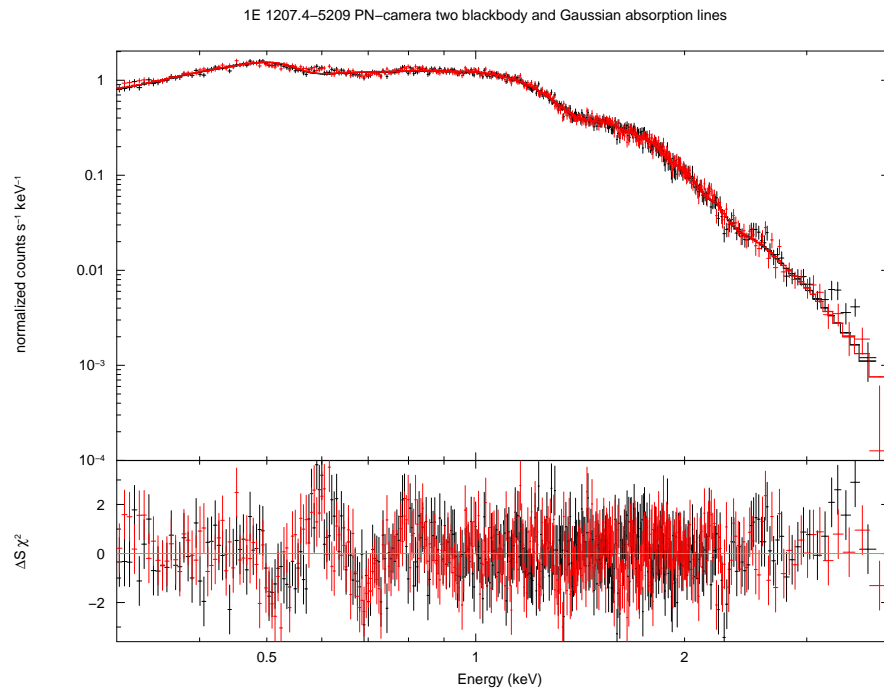


Figure 5.1. Spectra of 1E 1207.4-5209. Data from EPIC-PN cameras are shown with two blackbody and Gaussian absorption lines model.

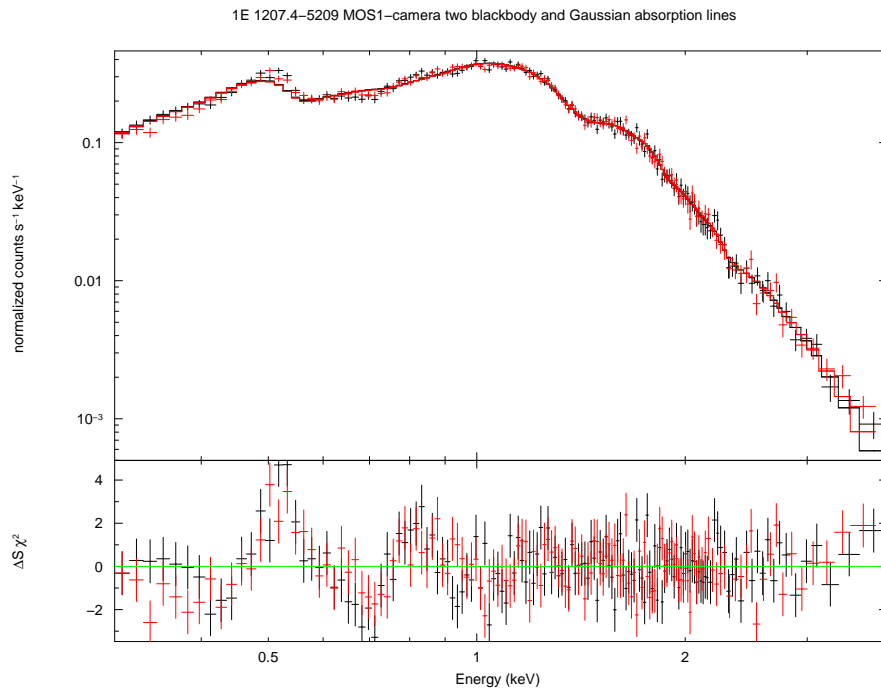


Figure 5.2. Spectra of 1E 1207.4-5209. Data from EPIC-MOS1 cameras are shown with two blackbody and Gaussian absorption lines model.

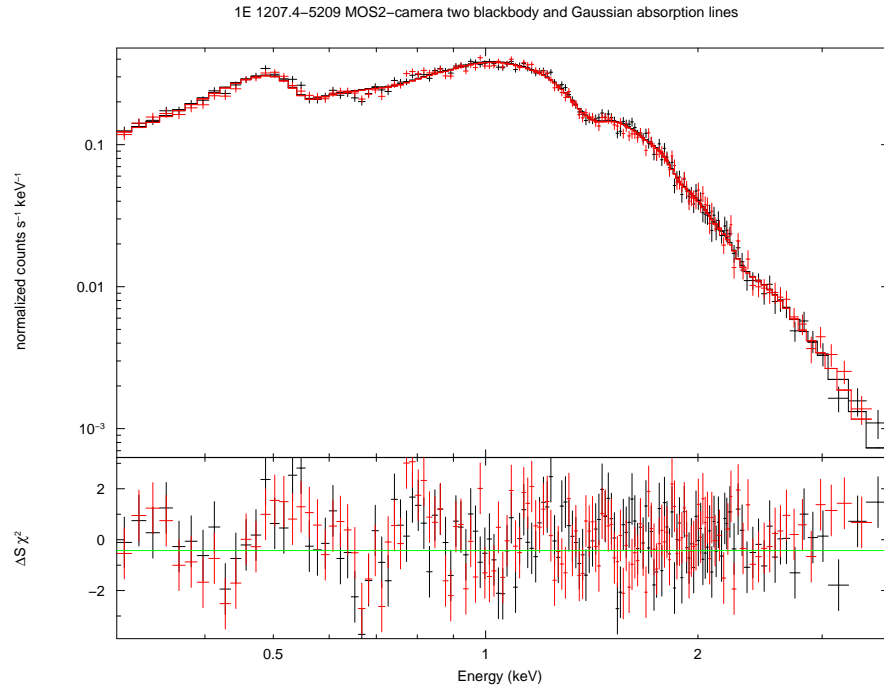


Figure 5.3. Spectra of 1E 1207.4-5209. Data from EPIC-MOS2 cameras are shown with two blackbody and Gaussian absorption lines model.

5.2. RX J0002+6246

The results of PN and PN, MOS1 and MOS2 simultaneously fitted data are represented in Table 5.2. The spectra were rebinned by *grppha* in order to have at least 40 counts per bin. The energy range was chosen to be 0.3-5.0 keV as the source is marginally detected beyond 5 keV. Single component black body or power law does not fit the data well. Black body plus black body and black body plus power law fits are equally acceptable, but the corresponding N_H of the latter is much larger than the SNR's N_H that the best fit is obtained by a two component black body (see Figure 5.4, Figure 5.5, Figure 5.6, Figure 5.7) with $kT_1=0.094$ keV, $kT_2=0.38$ keV and $N_H=7 \times 10^{21}$ cm^{-2} (comparable to the SNR's N_H).

Table 5.2. Spectral parameters of RX J0002+6246.

Parameter	PN		PN+MOS1+MOS2	
	BB+BB	BB+POW	BB+BB	BB+POW
$N_H(10^{22} \text{cm}^{-2})$	$0.70^{+0.05}_{-0.05}$	$0.85^{+0.12}_{-0.18}$	$0.72^{+0.06}_{-0.03}$	$0.87^{+0.13}_{-0.05}$
$kT_1(\text{keV})$	$0.37^{+0.06}_{-0.05}$		$0.38^{+0.05}_{-0.04}$	
$kT_2(\text{keV})$	$0.095^{+0.006}_{-0.005}$	$0.082^{+0.006}_{-0.003}$	$0.094^{+0.005}_{-0.003}$	$0.081^{+0.018}_{-0.014}$
Photon Index		$3.95^{+0.51}_{-0.46}$		$3.97^{+0.73}_{-0.63}$
$flux(\text{erg cm}^{-2} \text{s}^{-1})(0.3\text{-}5.0 \text{ keV})$	1.38×10^{-13}	1.42×10^{-13}	1.56×10^{-13}	1.57×10^{-13}
Reduced chi-squared	1.52	1.55	1.32	1.38
D.O.F.	28	28	35	35

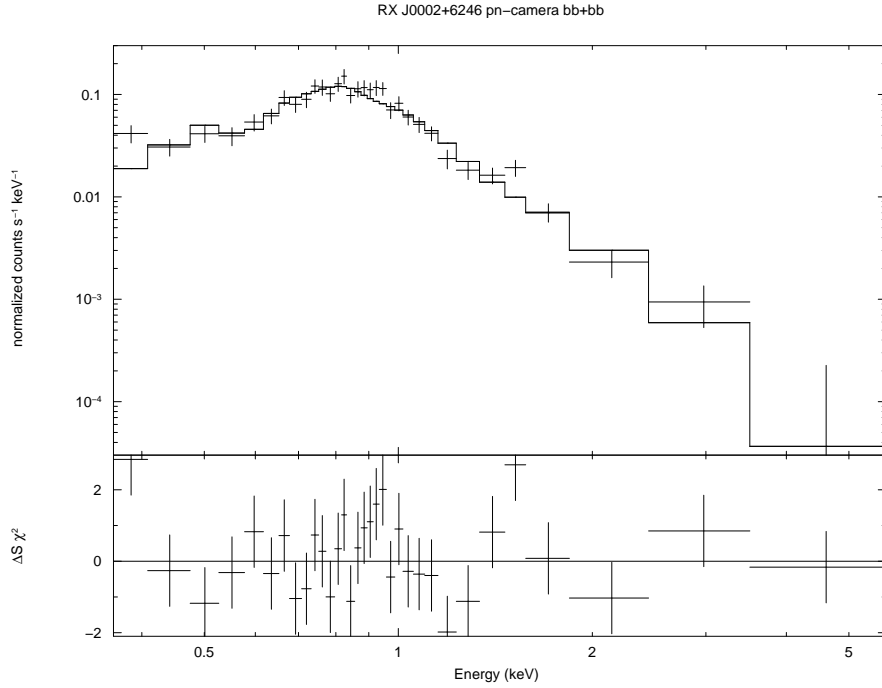


Figure 5.4. Spectra of RX J0002+6246. Data from EPIC-PN cameras are shown with two component blackbody model.

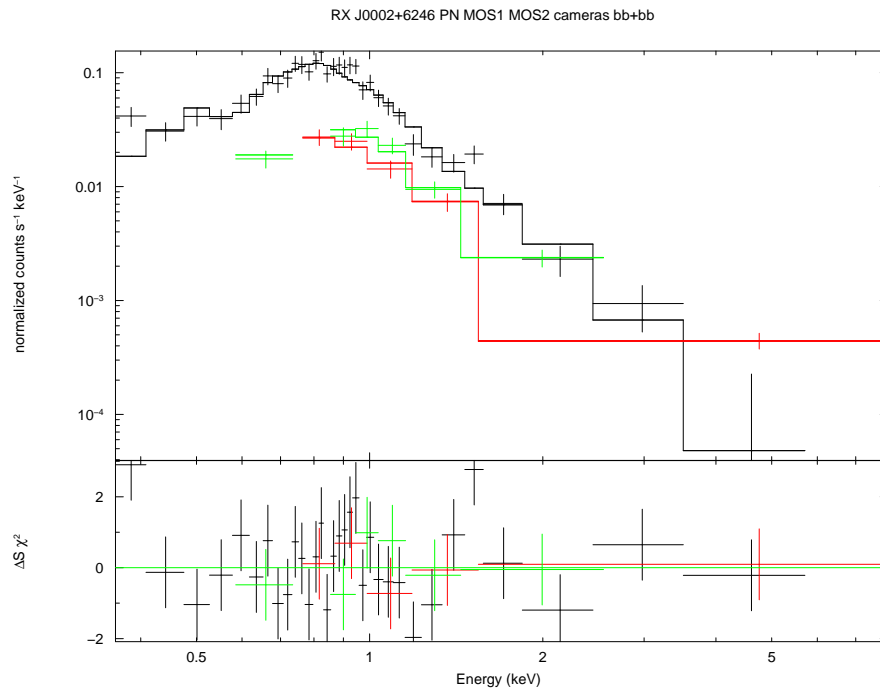


Figure 5.5. Spectra of RX J0002+6246. Data from EPIC-PN, MOS1 and MOS2 cameras simultaneously fitted two component blackbody model.

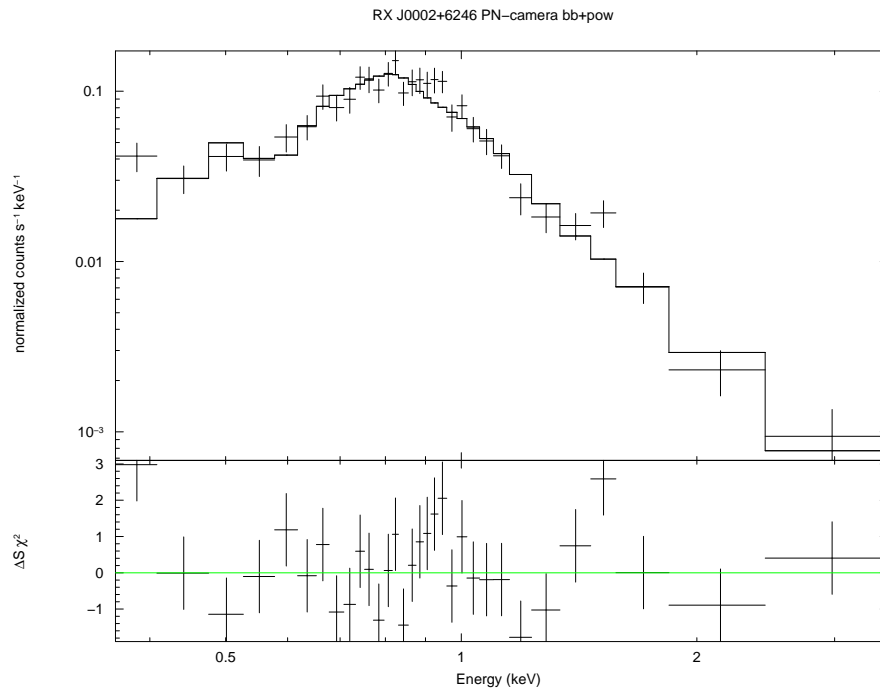


Figure 5.6. Spectra of RX J0002+6246. Data from EPIC-PN cameras are shown with blackbody and powerlaw model.

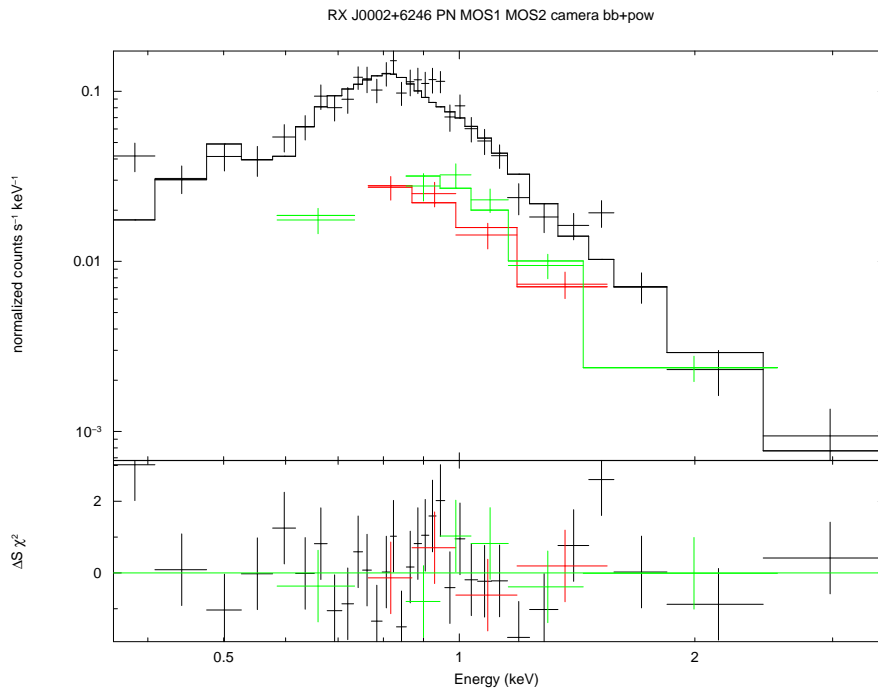


Figure 5.7. Spectra of RX J0002+6246. Data from EPIC-PN, MOS1 and MOS2 cameras are simultaneously fitted blackbody and powerlaw model.

5.3. RX J0822-4300

The results of PN and PN, MOS1 and MOS2 simultaneously fitted data are represented in Table 5.3. The spectra were rebinned by *grppha* in order to have at least 200 counts per bin. The energy range was chosen to be 0.3-5.0 keV as the source is marginally detected beyond 5 keV. Single component black body or power law does not fit the data well. Black body plus black body and black body plus power law fits are equally acceptable, but the corresponding N_H of the latter is about two times the SNR's N_H that the best fit is obtained by a two component black body (see Figure 5.8, Figure 5.9, Figure 5.10, Figure 5.11) with $kT_1=0.23$ keV, $kT_2=0.43$ keV and $N_H=5 \times 10^{21} \text{ cm}^{-2}$ (comparable to the SNR's N_H).

Table 5.3. Spectral parameters of RX J0822-4300.

Parameter	PN		PN+MOS1+MOS2	
	BB+BB	BB+POW	BB+BB	BB+POW
$N_H(10^{22} \text{cm}^{-2})$	$0.52^{+0.02}_{-0.03}$	$0.95^{+0.07}_{-0.06}$	$0.50^{+0.04}_{-0.03}$	$0.90^{+0.03}_{-0.05}$
$kT_1(\text{keV})$	$0.21^{+0.04}_{-0.01}$		$0.23^{+0.01}_{-0.02}$	
$kT_2(\text{keV})$	$0.42^{+0.01}_{-0.04}$	$0.39^{+0.01}_{-0.02}$	$0.43^{+0.02}_{-0.02}$	$0.38^{+0.01}_{-0.02}$
Photon Index		$4.97^{+0.21}_{-0.21}$		$4.62^{+0.10}_{-0.27}$
$flux(\text{ergs cm}^{-2} \text{s}^{-1})(0.3\text{-}5.0 \text{ keV})$	4.23×10^{-12}	4.24×10^{-12}	4.31×10^{-12}	4.32×10^{-12}
Reduced chi-squared	0.99	0.98	1.02	0.99
D.O.F.	269	269	352	352

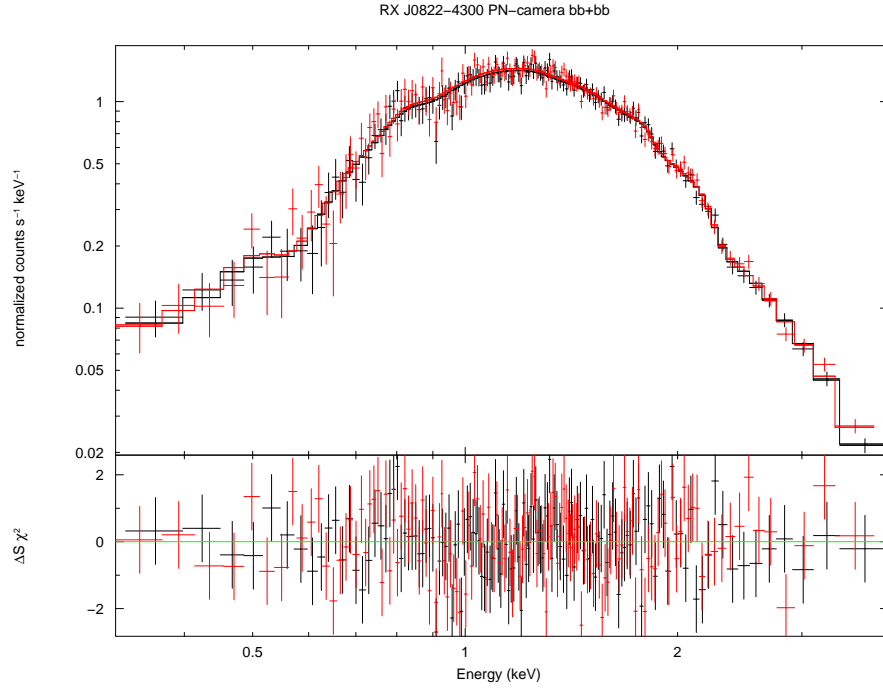


Figure 5.8. Spectra of RX J0822-4300. Data from EPIC-PN cameras are shown with two component blackbody model.

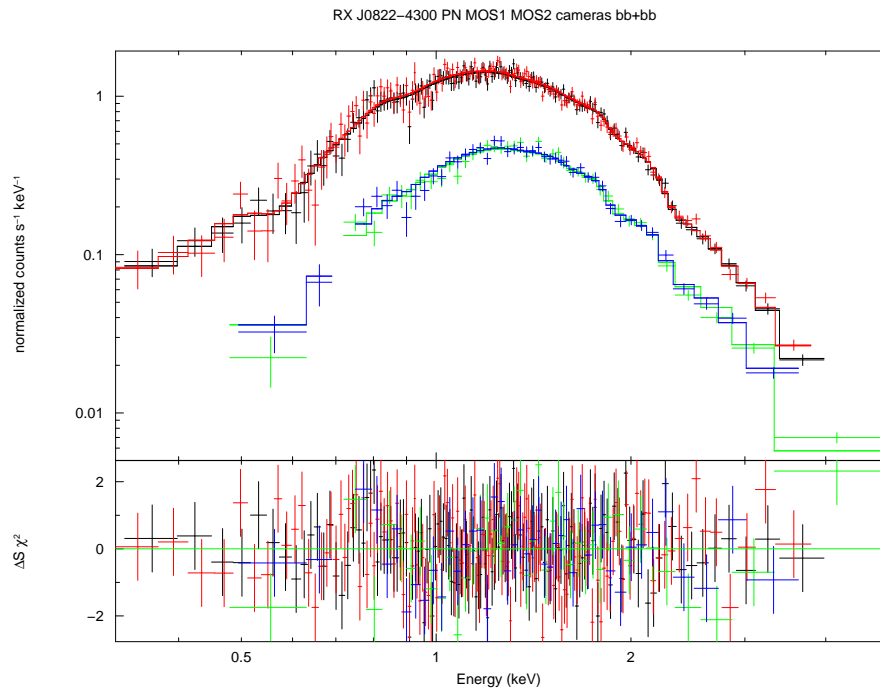


Figure 5.9. Spectra of RX J0822-4300. Data from EPIC-PN, MOS1 and MOS2 cameras are simultaneously fitted with two component blackbody model.

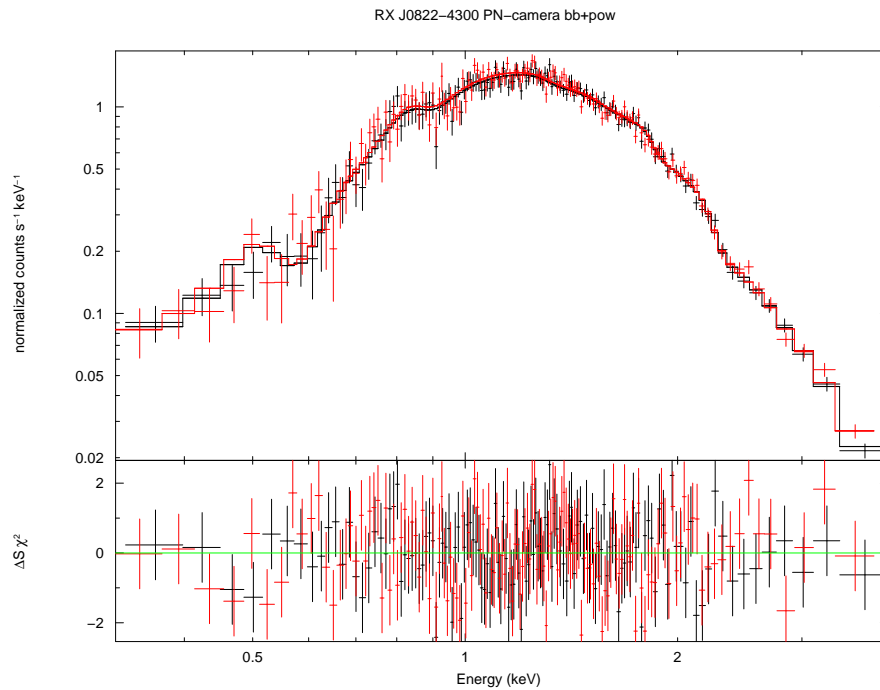


Figure 5.10. Spectra of RX J0822-4300. Data from EPIC-PN cameras are shown with blackbody and powerlaw model.

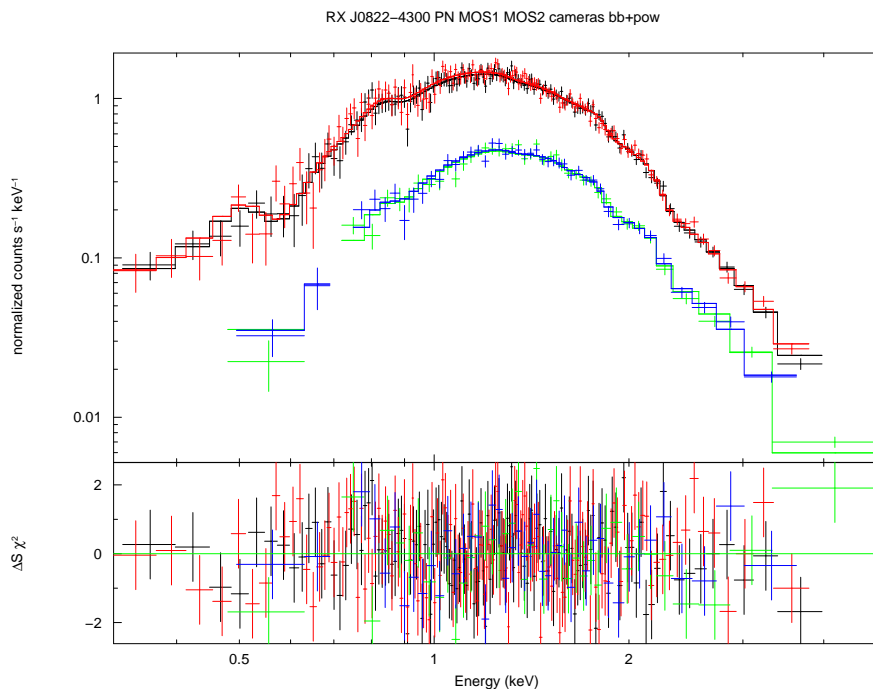


Figure 5.11. Spectra of RX J0822-4300. Data from EPIC-PN, MOS1 and MOS2 cameras are simultaneously fitted with blackbody and powerlaw model.

5.4. CXOUJ185238.6+004020

The results of PN and PN, MOS1 and MOS2 simultaneously fitted data are represented in Table 5.4. The spectra were rebinned by *grppha* in order to have at least 40 counts per bin. Black body and power law fits are equally acceptable, but the corresponding N_H of the latter is significantly larger than the SNR's N_H that the best fit is obtained by black body (see Figure 5.12, Figure 5.13, Figure 5.14, Figure 5.15) with $kT=0.46$ keV and $N_H=1.35 \times 10^{22}$ cm^{-2} (comparable to the SNR's N_H).

Table 5.4. Spectral parameters of CXOUJ185238.6+004020.

Parameter	PN		PN+MOS1+MOS2	
	BB	POW	BB	POW
$N_H(10^{22} \text{cm}^{-2})$	$1.15^{+0.22}_{-0.19}$	$2.97^{+0.49}_{-0.42}$	$1.35^{+0.15}_{-0.14}$	$3.19^{+0.36}_{-0.32}$
$kT(\text{keV})$	$0.49^{+0.03}_{-0.02}$		$0.46^{+0.02}_{-0.02}$	
Photon Index		$4.69^{+0.44}_{-0.40}$		$4.92^{+0.34}_{-0.31}$
$flux(\text{ergscm}^{-2}\text{s}^{-1})(0.7\text{-}5.0 \text{keV})$	1.94×10^{-13}	1.91×10^{-13}	2.10×10^{-13}	2.11×10^{-13}
Reduced chi-squared	0.83	0.94	0.83	0.94
D.O.F.	72	72	141	141

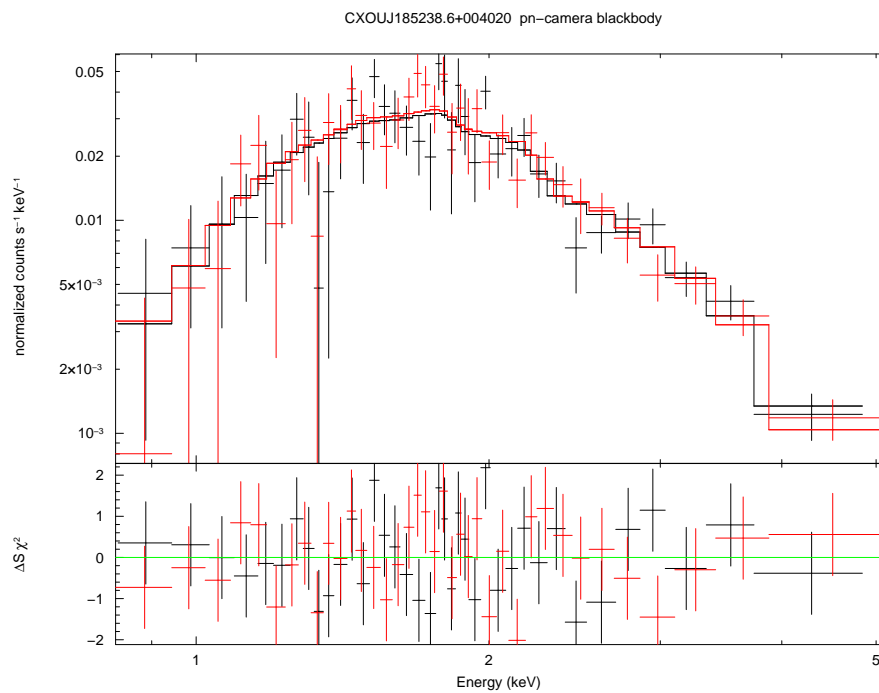


Figure 5.12. Spectra of CXOUJ185238.6+004020. Data from EPIC-PN cameras are shown with blackbody model.

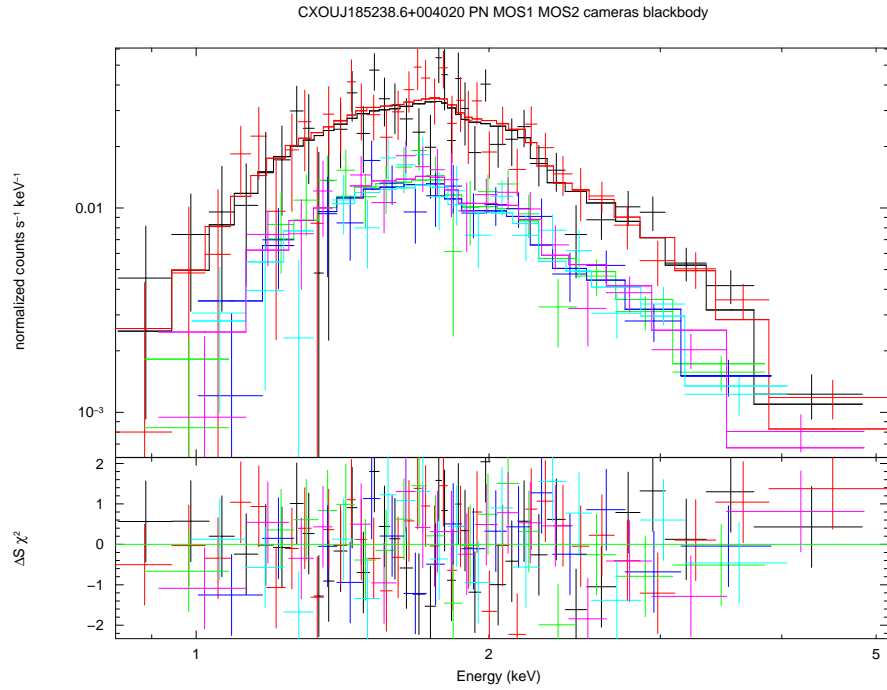


Figure 5.13. Spectra of CXOUJ185238.6+004020. Data from EPIC-PN, MOS1 and MOS2 cameras are simultaneously fitted with blackbody model.

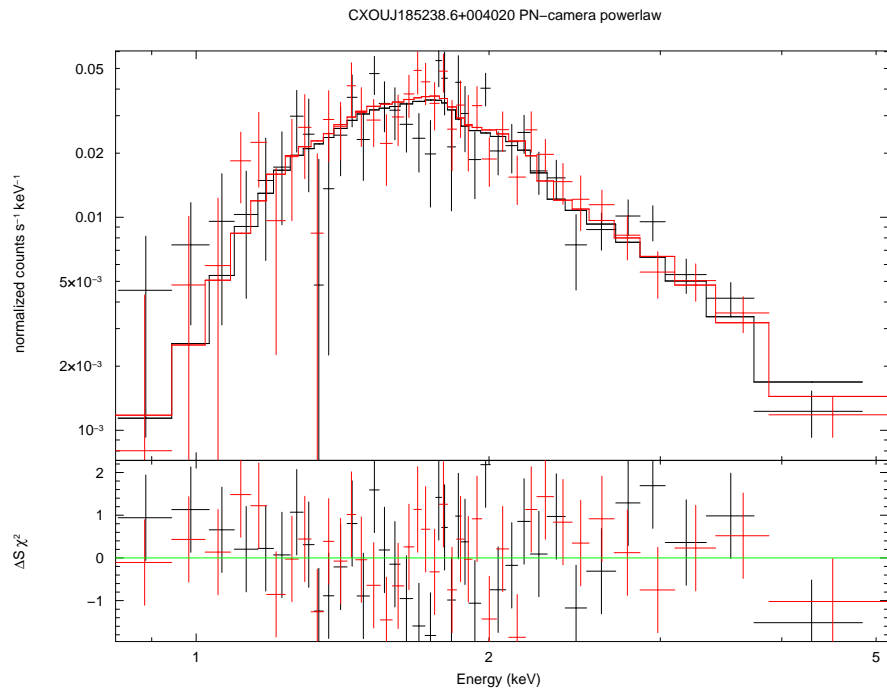


Figure 5.14. Spectra of CXOUJ185238.6+004020. Data from EPIC-PN cameras are shown with powerlaw model.

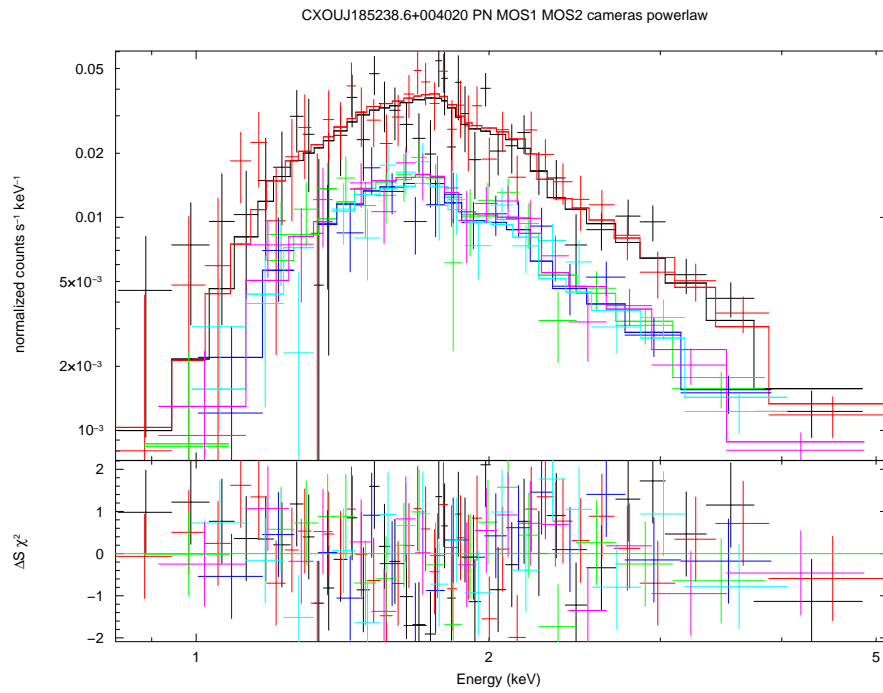


Figure 5.15. Spectra of CXOUJ185238.6+004020. Data from EPIC-PN, MOS1 and MOS2 cameras are simultaneously fitted with powerlaw model.

6. DISCUSSIONS AND CONCLUSIONS

1E 1207.4-5209 have some observational characteristics which can be used to classify the neutron stars which are similar to this radio-quiet X-ray pulsar. X-ray spectrum of 1E 1207.4-5209 includes 2 blackbody fits with no power-law component. There is no PWN around this X-ray source, though it is a young neutron star (age of the S-type SNR G296.5+10.0 is about 10-20 kyr). There is no detection of radio emission coming from this source similar to AXPs, SGRs and DTNSs. The characteristic age of the X-ray pulsar is much larger than the age of the SNR. Surface magnetic field of 1E 1207.4-5209 based on the resonant proton cyclotron line and its harmonics seen in its spectrum is 2 orders of magnitude larger than the B-field (perpendicular component of the surface magnetic field). There are rapid oscillations in the \dot{P} which can not be explained by glitches or noise. Large value of the ratio L_X/\dot{E} for 1E 1207.4-5209, unlike radio pulsars, is similar to some other radio-quiet neutron stars and magnetars.

The low value of \dot{E} can be used to explain why there is no PWN around this neutron star (i.e. why the SNR is S-type) as the formation of PWN strongly depends on the value of \dot{E} (Guseinov et al. 2005c). Such cases with low \dot{E} and no PWN do exist even among some other young pulsars and there would be no problem if τ and $t(\text{SNR})$ were comparable in the case of 1E 1207.4-5209 – SNR G296.5+10.0 pair. The large difference (about 2 orders of magnitude) between the ages might in principle be explained by assuming that this X-ray pulsar was born with a rotation period similar to its present P . Unfortunately, this explanation further creates significant problems on formation of neutron stars via core-collapse supernovae. Unless there exists a large extra torque which further spins down the newborn neutron star (which is not present in the core-collapse supernova models and simulations), it must have an initial rotation period which must be at least 10 times less than its present rotation period. So, if 1207 was born spinning with a conventional rotation period (about 10-20 ms), the braking of its rotation would be at lower values of \dot{P} compared to pure magneto-dipole radiation braking. In other words, the average braking index (assuming a power-law temporal evolution) should be much larger than $n=3$ case which is correct only if the

net torque on the pulsar is nothing but magneto-dipole radiation torque.

Another problem is related to the large difference between the magnetic field inferred from the proton cyclotron line and the perpendicular component of the surface dipole field B . Because of the discrepancy between the ages as discussed above, the huge difference in the magnetic field values can not be explained by a very small angle between the rotation and the magnetic axes.

An exponential B-decay model can be used to explain both discrepancies (i.e. related to the ages and the magnetic fields). Such a model can also be used to understand the anomalous oscillations in the \dot{P} of this X-ray pulsar. Furthermore, it is also possible to understand both the lack of PWN (i.e. the smallness of \dot{E} at a young age) and the lack of detection of radio emission (as the width of beaming emission at radio frequencies can be much smaller than the beam width in X-ray bands) based on such an exponential decay model. So, the lack of power-law component in the spectrum of 1207 is also explained by such a model.

In Sedrakian and Blaschke (2002) and Sedrakian and Shahabasyan (2007), the possibility of two different magnetic fields existing in neutron stars is discussed, the superposition of which will give the resultant field. According to their calculations, in addition to the relic magnetic field formed by the collapse of the progenitor star, there must also be a magnetic field formed by superconducting entrainment currents which was calculated to be on the order of 10^{12} G by Sedrakian et al.. Since this magnetic field must naturally be parallel to the rotation axis and as the relic magnetic field axis can have an arbitrary angle (α) with respect to the rotation axis, the resultant magnetic field (i.e. the superposition of the two magnetic fields) will be at an arbitrary angle from the rotation axis. So, if the relic field is comparable to or smaller than the entrainment-current-field, than the resultant field will have an axis close to the axis of rotation. On the other hand, if the relic field is the dominant one, then it is possible that the axis of the resultant field may be approximately perpendicular to the rotation axis in some cases. The smallness of α in most of the cases for radio pulsars is known from the observational data.

For 1207, the angle α seems to be close to zero ($B_{cyc} \cong 1.4 \times 10^{14}$ G and $B \cong 2.5 \times 10^{12}$ G). As discussed above, this very small α could be formed by a rapid approach of the surface field to the rotation axis. As the axis of the relic magnetic field approaches the rotation axis, the magnitude of the resultant surface magnetic field (i.e. the total magnetic field on the surface which is the superposition of the relic field and the field formed by the superconducting entrainment currents) increases and its component which is perpendicular to the rotation axis decreases in time. Since 1E 1207.4-5209 has most probably very high $B_{cyclotron}$ and comparably very low B (perpendicular component of the resultant surface magnetic field) and as this neutron star is observed as a pulsar, $B_{cyclotron}$ must be comparable to the resultant surface magnetic field which is increasing in time (or to the relic magnetic field as the magnetic field formed by the entrainment currents must be on the order of 10^{12} G on average). On the other hand, the actual low B value of 1E 1207.4-5209 as compared to the case of $n=3$ (see Fig2.1) can be explained by the exponential decay as this perpendicular component decreases in time based on the discrepancy between the age values.

The increase in the magnitude of the resultant surface magnetic field of 1E 1207.4-5209 must be very small if the relic field is actually much higher than the entrainment field, so that the $B_{cyclotron}$ and hence the magnitude of the present resultant surface magnetic field must be comparable to the magnitude of the initial resultant surface magnetic field. On the other hand, the decrease in the perpendicular component of the resultant surface magnetic field must be very large (about one order of magnitude) in a very short time interval ($\sim 10^4$ yr) compared to radio pulsar lifetimes. In the case of radio pulsars, the increase in the magnitude of the resultant surface magnetic field must be relatively large (up to a factor of about 1.5) based on the known B values of radio pulsars and the prediction on the average strength of the entrainment field, and the decrease in the perpendicular component of the field must exist on a much longer timescale. Comparing the magnetic field values of 1E 1207.4-5209 with the B values of most of the radio pulsars together with the age discrepancy for 1E 1207.4-5209 – SNR G296.5+10.0 pair (which also exists for several other pulsar – SNR pairs but without any clearly detected absorption lines) may be an evidence for the existence of two different magnetic fields for neutron stars; the relic field and the entrainment field.

The interaction between the superconducting entrainment currents and the relic field may be the reason for the decrease in α . Such a possible interaction between the two fields throughout the evolution of neutron stars with different initial intrinsic physical conditions has yet to be examined.

The rate of temporal decrease in α (and hence the evolution of the perpendicular component of the total surface dipole magnetic field) may depend on both the relic and hence the resultant magnetic field, the mass and the equation of state of the neutron star (it may also depend on the initial value of α). The changes in \dot{P} observed for 1E 1207.4-5209 may also be explained by oscillations in the magnetic dipole axis as it approaches the rotation axis. Such changes in \dot{P} must also exist in other 1207-like isolated radio-quiet X-ray pulsars.

The surface magnetic fields of accreting X-ray pulsars in X-ray binaries obtained from cyclotron line measurements are on the order of 10^{12} G (Coburn et al. 2002), that is comparable to the predicted surface magnetic fields due to the entrainment currents (Sedrakian and Blaschke 2002; Sedrakian and Shahabasyan 2007), and the B values of recycled millisecond pulsars are several orders of magnitude smaller (see Bisnovatyi-Kogan and Komberg 1976, who gave the first reliable explanation for the magnetic field decay in X-ray binaries by accretion and the formation of recycled millisecond pulsars). The surface magnetic field in the case of X-ray binaries most probably decreases because of the plasma falling upon the surface of the neutron star during the accretion process (Bisnovatyi-Kogan and Fridman 1969; Amnuel and Guseinov 1969; Bisnovatyi-Kogan and Komberg 1976; Bisnovatyi-Kogan 2007). A decrease in the resultant surface field because of accretion and maybe also a decrease in the value of α (but on a much longer timescale compared to the 1E 1207.4-5209 case) may explain the measured conventional 10^{12} G magnetic field values of X-ray pulsars in binary systems and the very low perpendicular components of the resultant surface field of recycled millisecond pulsars.

A rapid B-decay naturally leads to a very short lifetime as an X-ray pulsar for 1207-like objects. The birth rate of 1207-like X-ray pulsars must be about 20-30%

of the total supernova rate (excluding type-Ia supernovae as this type of explosion most probably does not lead to formation of a neutron star) taking into consideration that the lifetime of such sources as X-ray pulsars must be about 2×10^4 yr because of rapid B-decay (see Guseinov et al. 2005c on the birth rates of different types of isolated neutron stars including dim radio quiet neutron stars some of which seem to be 1207-like objects based on the existing observational data). After the axis of the resultant surface magnetic field becomes parallel to the rotation axis, the neutron star will continue its evolution as an X-ray source (but not a pulsar). It will still be possible to observe such a neutron star in X-ray bands if it is not located far away from the Sun. Some radio-quiet thermal neutron stars (which are pure black body emitters with absolutely no power-law component) nearby the Sun may be descendants of 1207-like X-ray pulsars. If this is true, the high birth rate of DTNSs can be explained easily.

In this thesis, the X-ray spectra of 1E 1207.4-5209, RX J0002+6246, RX J0822-4300 and CXOU J185238.6+004020 were derived. The X-ray spectrum of RX J0002+6246 was fitted using XMM-Newton data for the first time. The results of X-ray fitting of the remaining three neutron stars are in accordance with the values given in the literature. 1207-like nature of three XDRQNSs was for the first time identified in this work based on the common observational properties of these sources as discussed above.

Analysis of long and precise timing observations of RX J0002+6246, RX J0822-4300 and CXOU J185238.6+004020 are needed to further clarify the nature of these sources, which I plan to do as future work.

REFERENCES

- Allakhverdiev, A. O., O. H. Guseinov and F. K. Kasumov, 1985, *Astrophysics and Space Science*, 115, 1.
- Annuel, P. R. and O. H. Guseinov, 1969, *Astronomicheskii Tsirkular*, no.574.
- Ankay, A., O. H. Guseinov and S. O. Tagieva, 2004, *Astronomical and Astrophysical Transactions*, 23, 503.
- Ankay, A., A. M. Ankay and E. N. Ercan, 2007, *International Journal of Modern Physics D*, 16, 619.
- Arnaud, K. et al., 2006, *An XSPEC User's Guide for version 12.2.1*
- Bisnovatyi-Kogan, G. S. and A. M. Fridman, 1969, *Pis'ma v Astronomicheskii Zhurnal*, 46, 721.
- Bisnovatyi-Kogan, G. S. and B. V. Komberg, 1976, *Soviet Astronomy Letters*, 2, 130.
- Bisnovatyi-Kogan, G. S., 2007, "Evolutions of Neutron Stars and Their Magnetic Fields" in *Neutron Stars, Supernovae and Supernova Remnants*, edi. Efe Yazgan, Askin Ankay and Oktay H. Guseinov, Nova Science Publishers (ISBN: 1-60021-548-3).
- Blair, W. P., J. C. Raymond, K. S. Long and G. A. Kriss, 1995, *Astrophysical Journal*, 454, L35.
- Braun, R., W. M. Goss and A. G. Lyne, 1989, *Astrophysical Journal*, 340, 355.

- Brazier, K. T. S., G. Kanbach, A. Carraminana, J. Guichard and M. Merck, 1996, Monthly Notices of the Royal Astronomical Society, 281, 1033.
- Brazier, K. T. S. and S. Johnston, 1999, Monthly Notices of the Royal Astronomical Society, 305, 671.
- Charles, P. A. and M. J. Coe, 2003, astro-ph/0308020v2.
- Coburn, W., W. A. Heindl, R. E. Rothschild, D. E. Gruber, I. Kreykenbohm, J. Wilms, P. Kretschmar and R. Staubert, 2002, Astrophysical Journal, 580, 394.
- Dechristopher, B. M. and P. F. Winkler, 1994, American Astronomical Society, 26, 951.
- DeLuca, A., S. Mereghetti, P. A. Caraveo, R. P. Mignani, W. Becker and G. F. Bignami, 2003, Radio Pulsars, ASP Conf. Series, eds. M. Bailes, D. J. Nice and S. E. Thorsett.
- Duncan, R. C. and C. Thompson, 1992, Astrophysical Journal, 392, L9.
- Ehle, M. et al., 2006, XMM-Newton Users Handbook Issue 2.4.
- Fang, R. and L. Z. Ruffini, 1983, Basic Concepts in Relativistic Astrophysics, World Sci. Publ. .
- Frail, D. A. and T. R. Clifton, 1989, Astrophysical Journal, 336, 854.
- Geppert, U. and M. Rheinhardt, 2002, Astronomy and Astrophysics, 392, 1015.
- Gotthelf, E. V., J. P. Halpern and F. D. Seward, 2005, Astrophysical Journal, 627, 390.

- Green, D. A., 2006, A Catalogue of Galactic Supernova Remnants,
<http://www.mrao.cam.ac.uk/surveys/snrs/> .
- Guseinov, O. H., E. Yazgan, A. Ankay and S. O. Tagieva, 2003a, International Journal of Modern Physics D, 12, 1.
- Guseinov, O. H., E. Yazgan, S. O. Tagieva and S. Ozkan, 2003b, Revista Mexicana de Astronomia y Astrofisica, 39, 267.
- Guseinov, O. H., A. Ankay and S. O. Tagieva, 2003c, Astronomical and Astrophysical Transactions, 22, 273.
- Guseinov, O. H., A. Ankay and S. O. Tagieva, 2003d, Serbian Astronomical Journal, 167, 93.
- Guseinov, O. H., A. Ankay and S. O. Tagieva, 2004a, Serbian Astronomical Journal, 168, 55.
- Guseinov, O. H., A. Ankay and S. O. Tagieva, 2004b, International Journal of Modern Physics D, 13, 1805.
- Guseinov, O. H., A. Ankay and S. O. Tagieva, M. O. Taskin, 2004c, International Journal of Modern Physics D, 13, 197
- Guseinov, O. H., A. Ankay and S. O. Tagieva, 2005a, International Journal of Modern Physics D, 14, 1465.
- Guseinov, O. H., A. Ankay and S. O. Tagieva, 2005b, Astrophysics and Space Science, 298, 553.
- Guseinov, O. H., A. Ankay and S. O. Tagieva, 2005c, International Journal of Modern Physics D, 14, 643.

- Haberl, F., 2005, MPE Report, Vol.288, p.39.
- Halpern, J. P., E. V. Gotthelf, F. Camilo and D. J. Helfand, 2004, *Astrophysical Journal*, 612, 398.
- Halpern, J. P., E. V. Gotthelf, R. H. Becker, D. J. Helfand and R. L. White, 2005, *Astrophysical Journal*, 632, L29.
- Halpern, J. P., E. V. Gotthelf, F. Camilo and F. D. Seward, 2007, astro-ph/0705.0978v1.
- Hailey C. J. and W. W. Craig, 1995, *Astrophysical Journal*, 455, L151.
- Hansen, B. M. S. and E. S. Phinney, 1996, American Astronomical Society, 189th AAS Meeting, Vol.28, p.1368.
- Hui, C. Y. and W. Becker, 2006a, *Astronomy and Astrophysics*, 454, 543.
- Hui, C. Y. and W. Becker, 2006b, *Astronomy and Astrophysics*, 457, L33.
- Humphreys, R. M., 1978, *Astronomy and Astrophysics Supplement Series*, 38, 309.
- Kaspi, V. M., R. N. Manchester, S. Johnston, A. G. Lyne and N. D'Amico, 1996, *Astronomical Journal*, 111, 2028.
- Kaspi, V. M., F. P. Gavriil, P. M. Woods, J. B. Jensen, M. S. E. Roberts and D. Chakrabarty, 2003, *Astrophysical Journal*, 588, L93.
- Kirsch, M., 2006, XMM-Science Ops Centre Technical Note, XMM-SOC-CAL-TN-0018.
- Lipunov, V. M., 1992, *Astrophysics of Neutron Stars*, Springer Verlag.

- Loiseau, N. et al., 2006, Users Guide to the XMM-Newton Science Analysis System Issue 4.0.
- Lyne, A. G. and F. Graham-Smith, 2006, Pulsar Astronomy, Cambridge University Press.
- Malone, R. C., 1974, PhD Thesis, Cornell University, Ithaca, New York.
- Melnik A. M. and Yu. N. Efremov, 1995, *Astronomical Letters*, 21, 10.
- Petre, R., C. M. Becker and P. F. Winkler, 1996, *Astrophysical Journal*, 465, L43.
- Reynoso, E. M., G. M. Dubner, W. M. Goss and E. M. Arnal, 1995, *Astronomical Journal*, 110, 318.
- Reynoso E. M., A. J. Green, S. Johnston, W. M. Goss, G. M. Dubner and E. B. Giacani, 2004, *Publications of the Astronomical Society of Australia*, 21, 82.
- Sedrakian, D. M. and D. Blaschke, 2002, *Astrophysics*, 45, 166.
- Sedrakian, D. M. and K. M. Shahabasyan, 2007, "The Magnetic Field of Pulsars" in *Neutron Stars, Supernovae and Supernova Remnants*, edi. Efe Yazgan, Askin Ankey and Oktay H. Guseinov, Nova Science Publishers (ISBN: 1-60021-548-3).
- Seward, F. D., P. O. Slane, R. K. Smith and M. Sun, 2003, *Astrophysical Journal*, 584, 414.
- Shapiro and Teukolsky, 2004, *Black Holes, White Dwarfs, and Neutron Stars*, WILEY-VCH Verlag.
- Slane, P., E. R. Zimmerman, J. P. Hughes, F. D. Seward, B. M. Gaensler and M. J. Clarke, 2004, *Astrophysical Journal*, 601, 1045.

- Strueder, L., U. Briel, K. Dennerl, et al., 2001, *Astronomy and Astrophysics*, 365, L18.
- Sun, M., F. D. Seward, R. K. Smith and P. O. Slane, 2004, *Astrophysical Journal*, 605, 742.
- Tauris, T. M. and R. N. Manchester, 1998, *Monthly Notices of the Royal Astronomical Society*, 298, 625.
- Thompson, C. and R. C. Duncan, 1995, *Monthly Notices of the Royal Astronomical Society*, 275, 255.
- Thompson, C. and R. C. Duncan, 1996, *Astrophysical Journal*, 473, 322.
- Tsuruta, S., 1974, *Cooling of Dense Stars*, IAU Symposium 53, p.456.
- Tsuruta, S., 1979, *Thermal Properties and Detectability of Neutron Stars - I. Cooling and Heating of Neutron Stars*, *Phys. Rept.* 56, 237.
- Turner, M. J. L., A. Abbey, M. Arnaud, et al., 2001, *Astronomy and Astrophysics*, 365, L27.
- Winkler, P. F., C. R. Canizares, G. W. Clark, et al., 1981a, *Astrophysical Journal*, 245, 574.
- Winkler, P. F., C. R. Canizares, G. W. Clark, et al., 1981b, *Astrophysical Journal*, 246, L27.
- Winkler, P. F., J. H. Tuttle, R. P. Kirshner and M. J. Irwin, 1988, *Supernova Remnants and the Interstellar Medium*, ed. R. S. Roger and T. L. Landecker, p.65.
- Woermann, B., M. J. Gaylard and R. Otrupcek, 2000, *Monthly Notices of the Royal Astronomical Society*, 317, 421.

Zavlin, V. E., J. Trumper and G. G. Pavlov, 1999, *Astrophysical Journal*, 525, 959.